

Variational approach for electrolyte solutions: from dielectric interfaces to charged nanopores

Sahin Buyukdagli*, Manoel Manghi†, and John Palmeri‡

Université de Toulouse; UPS;

Laboratoire de Physique Théorique (IRSAMC); F-31062 Toulouse, France and

CNRS; LPT (IRSAMC); F-31062 Toulouse, France

(Dated: October 23, 2018)

A variational theory is developed to study electrolyte solutions, composed of interacting point-like ions in a solvent, in the presence of dielectric discontinuities and charges at the boundaries. Three important and non-linear electrostatic effects induced by these interfaces are taken into account: surface charge induced electrostatic field, solvation energies due to the ionic cloud, and image charge repulsion. Our variational equations thus go beyond the mean-field theory, or weak coupling limit, where thermal fluctuations overcome electrostatic correlations, and allows one to reach the opposite strong coupling limit, where electrostatic interactions induced by interfaces dominate. The influence of salt concentration, ion valency, dielectric jumps, and surface charge is studied in two geometries. i) A single neutral dielectric interface (e.g. air–water or electrolyte–membrane) with an asymmetric electrolyte. A charge separation and thus an electrostatic field gets established due to the different image charge repulsions for coions and counterions. Both charge distributions and surface tension are computed and compared to previous approximate calculations. For symmetric electrolyte solutions close to a charged surface, two zones are characterized. In the first one, in contact with the surface and with size proportional to the logarithm of the coupling parameter, strong image forces and strong coupling impose a total ion exclusion, while in the second zone the mean-field approach applies. ii) A symmetric electrolyte confined between two dielectric interfaces as a simple model of ion rejection from nanopores in membranes. The competition between image charge repulsion and attraction of counterions by the membrane charge is studied. For small surface charge, the counterion partition coefficient decreases with increasing pore size up to a critical pore size, contrary to neutral membranes. For larger pore sizes, the whole system behaves like a neutral pore. For strong coupling and small pore size, coion exclusion is total and the counterion partition coefficient is solely determined by global electroneutrality. A quantitative comparison is made with a previous approach, where image and surface charge effects were smeared out in the pore. It is shown that the variational method allows one to go beyond the constant Donnan potential approximation, with deviations stronger at high ion concentrations or small pore sizes. The prediction of the variational method is also compared with MC simulations and a good agreement is observed.

PACS numbers: 03.50.De,87.16.D-,68.15.+e

I. INTRODUCTION

The first experimental evidence for the enhancement of the surface tension of inorganic salt solutions compared to that of pure water was obtained more than eight decades ago [1, 2]. Wagner proposed the correct physical picture [3] by relating this effect to image forces that originate from the dielectric discontinuity and act on ions close to the water–air interface. He also correctly pointed out the fundamental importance of the ionic screening of image forces and formulated a theoretical description of the problem by establishing a differential equation for the electrostatic potential and solving it numerically to compute the surface tension. Using series expansions, Onsager and Samaras found the celebrated limiting law [4] that relates the surface tension of symmetric electrolytes to the bulk electrolyte density at low salt concentration.

However, it is known that the consideration of charge asymmetry leads to a technical complication. Indeed, image charge repulsion, whose amplitude is proportional to the square of ion valency, leads to a split of concentration profiles for ions of different charge, which in turn causes a local violation of the electroneutrality and induces an electrostatic field close to a neutral dielectric interface. Bravina derived five decades ago a Poisson-Boltzmann type of equation for this field [5] and used several approximations in order to derive integral expressions for the charge distribution and the surface tension.

These image charge forces play also a key role in slit-like nanopores which are model systems for studying ion rejection and nanofiltration by porous membranes (see the review [6] and references therein, and [7] for a review of nano-fluidics). Several results have been found in this geometry and also for cylindrical nanopores beyond the mean-field approach (using the Debye closure and the BBGKY hierarchical equations) and averaging all dielectric and charge effects over the pore cross section. Within these two approximations, the salt reflection coefficient has been studied as a function of the pore size, the bulk

*email: buyuk@irsamc.ups-tlse.fr

†email: manghi@irsamc.ups-tlse.fr

‡email: john.palmeri@irsamc.ups-tlse.fr

salt concentration and the pore surface charge.

More precisely, the strength of electrostatic correlations of ions in the presence of charged interfaces *without dielectric discontinuity* is quantified by one unique coupling parameter

$$\Xi = 2\pi q^3 \ell_B^2 \sigma_s \quad (1)$$

where q is the ion valency, and σ_s the fixed surface charge [8–10]. The Bjerrum length in water for monovalent ions, $\ell_B = e^2/(4\pi\epsilon_w k_B T) \approx 0.7$ nm (ϵ_w is the dielectric permittivity of water) is defined as the distance at which the electrostatic interaction between two elementary charges is equal to the thermal energy $k_B T$. The second characteristic length is the Gouy-Chapman length $\ell_G = 1/(2\pi q \ell_B \sigma_s)$ defined as the distance at which the electrostatic interaction between a single ion and a charged interface is equal to $k_B T$. The coupling parameter can be reexpressed in terms of these two lengths as $\Xi = q^2 \ell_B / \ell_G$. On the one hand, the limit $\Xi \rightarrow 0$, called the weak coupling (WC) limit, is where the physics of the Coulomb system is governed by the mean-field or Poisson-Boltzmann (PB) theory, and thermal fluctuations overcome electrostatic interactions. It describes systems characterized by a high temperature, low ion valency or weak surface charge. On the other hand, $\Xi \rightarrow \infty$ is the strong coupling (SC) limit, corresponding to low temperature, high valency of mobile ions or strong surface charge. In this limit, ion-charged surface interactions control the ion distribution perpendicularly to the interface. For single interface and slab geometries, several perturbative approaches going beyond the WC limit [11] or below the SC limit [8, 12, 13] have been developed. Although these calculations were able to capture important phenomena such as charge renormalization [14], ion specific effects at the water-air interface [15, 16], Manning condensation [17], effect of monopoles [18] or attraction between similarly charged objects, they also showed slow convergence properties, which indicates the inability of high-order expansions to explore the intermediate regime, $\Xi \simeq 1$. This is quite frustrating since the common experimental situation usually corresponds to the range $0.1 < \Xi < 10$ where neither WC nor SC theory is totally adequate.

Consequently, a non-perturbative approach valid for the whole range of Ξ is needed. A first important attempt in this direction has been made by Netz and Orland [19] who derived variational equations within the primitive model for point-like ions and solved them at the mean-field level in order to illustrate charge renormalization effect. Interestingly, these differential equations are equivalent to the closure equations established in the context of electrolytes in nanopores [6]. They are too complicated to be solved analytically or even numerically for general Ξ . A few years later, Curtis and Lue [20] and Hatlo *et al.* [21] investigated the partition of symmetric electrolytes at neutral dielectric surfaces using a similar variational approach (see also the review [22]). They have also recently proposed a new variational scheme based on

a hybrid low fugacity and mean-field expansion [23], and showed that their approach agrees well with Monte-Carlo simulation results for the counterions-only case. However, this method is quite difficult to handle, and one has to solve two coupled variational equations, i.e. a sixth order differential equation for the external potential together with a second algebraic equation. Within this approach, these authors generalized the study of ion-ion correlations for counterions close to a charged dielectric interface, first done by Netz in the WC and SC limits [24], to intermediate values of Ξ . They also studied an electrolyte between two charged surfaces without dielectric discontinuities at the pore boundary, in two cases: counterions only and added salt, handled at the mean-field level [25]. Although this simplification allows one to focus exclusively on ion-ion correlations induced by the surface charge, the dielectric discontinuity can not be discarded in synthetic or biological membranes. Indeed, it is known that image forces play a crucial role in ion filtration mechanisms [6]. The main goal of this work is to propose a variational analysis which is simple enough to intuitively illustrate ionic exclusion in slit pores, by focusing on the competition between image charge repulsion and surface charge interaction. Moreover, our approach allows us to connect nanofiltration studies [26–28] with field-theoretic approaches of confined electrolyte solutions within a generalized Onsager-Samaras approximation [4] characterized by a uniform variational screening length. This variational parameter takes into account the interaction with both image charge and surface charge. We also compare the prediction of the variational theory with Monte-Carlo simulations [29] and show that the agreement is good.

The paper is organized as follows. The variational formalism for Coulombic systems in the presence of dielectric discontinuities is introduced in Section II. Section III deals with a single interface. We show that the introduction of simple variational potentials allows one to fully account for the physics of asymmetric electrolytes at dielectric interfaces (e.g. water–air, liquid–liquid and liquid–solid interfaces, see ref. [30]), first studied by Bravina [5] using several approximations, as well as the case of charged surfaces. In Section IV, the variational approach is applied to a symmetric electrolyte confined between two dielectric surfaces in order to investigate the problem of ion rejection from membrane nanopores. Using restricted variational potentials, we show that due to the interplay between image charge repulsion and direct electrostatic interaction with the charged surface, the ionic partition coefficient has a non-monotonic behaviour as a function of pore size.

II. VARIATIONAL CALCULATION

In this section, the field theoretic variational approach for many body systems composed of point-like ions in the presence of dielectric interfaces is presented. Since the field theoretic formalism as well as the first order varia-

tional scheme have already been introduced in previous works [19, 20], we only illustrate the general lines.

The grand-canonical partition function of p ion species in a liquid of spatially varying dielectric constant $\epsilon(\mathbf{r})$ is

$$\mathcal{Z} = \prod_{i=1}^p \sum_{N_i=0}^{\infty} \frac{e^{N_i \mu_i}}{N_i! \lambda_t^{3N_i}} \int \prod_{j=1}^{N_i} d\mathbf{r}_{ij} e^{-(H-E_s)} \quad (2)$$

where λ_t is the thermal wavelength of an ion, μ_i denotes the chemical potential and N_i the total number of ions of type i . For sake of simplicity, all energies are expressed in units of $k_B T$. The electrostatic interaction is

$$H = \frac{1}{2} \int d\mathbf{r}' d\mathbf{r} \rho_c(\mathbf{r}) v_c(\mathbf{r}, \mathbf{r}') \rho_c(\mathbf{r}') \quad (3)$$

where ρ_c is the charge distribution (in units of e)

$$\rho_c(\mathbf{r}) = \sum_{i=1}^p \sum_{j=1}^{N_i} q_i \delta(\mathbf{r} - \mathbf{r}_{ij}) + \rho_s(\mathbf{r}), \quad (4)$$

and q_i denotes the valency of each species, $\rho_s(\mathbf{r})$ stands for the fixed charge distribution and $v_c(\mathbf{r}, \mathbf{r}')$ is the Coulomb potential whose inverse is defined as

$$v_c^{-1}(\mathbf{r}, \mathbf{r}') = -\frac{k_B T}{e^2} \nabla [\epsilon(\mathbf{r}) \nabla \delta(\mathbf{r} - \mathbf{r}')] \quad (5)$$

where $\epsilon(\mathbf{r})$ is a spatially varying permittivity. The self-energy of mobile ions, which is subtracted from the total electrostatic energy, is

$$E_s = \frac{v_c^b(0)}{2} \sum_{i=1}^p N_i q_i^2 \quad (6)$$

where $v_c^b(\mathbf{r}) = \ell_B/r$ is the bare Coulomb potential for $\epsilon(\mathbf{r}) = \epsilon_w$. After performing a Hubbard-Stratonovitch transformation and the summation over N_i in Eq. (2), the grand-canonical partition function takes the form of a functional integral over an imaginary electrostatic auxiliary field $\phi(\mathbf{r})$, $\mathcal{Z} = \int \mathcal{D}\phi e^{-H[\phi]}$. The Hamiltonian is

$$H[\phi] = \int d\mathbf{r} \left[\frac{[\nabla \phi(\mathbf{r})]^2}{8\pi \ell_B(\mathbf{r})} - i\rho_s(\mathbf{r})\phi(\mathbf{r}) - \sum_i \lambda_i e^{\frac{q_i^2}{2} v_c^b(0) + i q_i \phi(\mathbf{r})} \right] \quad (7)$$

where a rescaled fugacity

$$\lambda_i = e^{\mu_i} / \lambda_t^3 \quad (8)$$

has been introduced. The variational method consists in optimizing the first order cumulant

$$F_v = F_0 + \langle H - H_0 \rangle_0. \quad (9)$$

where averages $\langle \dots \rangle_0$ are to be evaluated with respect to the most general Gaussian Hamiltonian [19],

$$H_0[\phi] = \frac{1}{2} \int_{\mathbf{r}, \mathbf{r}'} [\phi(\mathbf{r}) - i\phi_0(\mathbf{r})] v_0^{-1}(\mathbf{r}, \mathbf{r}') [\phi(\mathbf{r}') - i\phi_0(\mathbf{r}')] \quad (10)$$

and $F_0 = -\frac{1}{2} \text{tr} \ln v_0$. The variational principle consists in looking for the optimal choices of the electrostatic kernel $v_0(\mathbf{r}, \mathbf{r}')$ and the average electrostatic potential $\phi_0(\mathbf{r})$ which extremize the variational grand potential Eq. (9). The variational equations $\delta F_v / \delta v_0^{-1}(\mathbf{r}, \mathbf{r}') = 0$ and $\delta F_v / \delta \phi_0(\mathbf{r}) = 0$, for a symmetric electrolyte and $\epsilon(\mathbf{r}) = \epsilon_w$, yield

$$\Delta \phi_0(\mathbf{r}) - 8\pi \ell_B q \lambda e^{-\frac{q^2}{2} W(\mathbf{r})} \sinh[q\phi_0(\mathbf{r})] = -4\pi \ell_B \rho_s(\mathbf{r}) \quad (11)$$

$$-\Delta v_0(\mathbf{r}, \mathbf{r}') + 8\pi \ell_B q^2 \lambda e^{-\frac{q^2}{2} W(\mathbf{r})} \cosh[q\phi_0(\mathbf{r})] v_0(\mathbf{r}, \mathbf{r}') = 4\pi \ell_B \delta(\mathbf{r} - \mathbf{r}'). \quad (12)$$

where we have defined

$$W(\mathbf{r}) \equiv \lim_{\mathbf{r} \rightarrow \mathbf{r}'} [v_0(\mathbf{r}, \mathbf{r}') - v_c^b(\mathbf{r} - \mathbf{r}')] \quad (13)$$

whose physical signification will be given below. The second terms on the LHS of Eq. (11) and of Eq. (12) have simple physical interpretations: the former is $4\pi \ell_B$ times the local ionic charge density and the latter is $4\pi \ell_B q^2$ times the local ionic concentration. The relations Eqs. (11)–(12) are respectively similar in form to the non-linear Poisson-Boltzmann (NLPB) and Debye-Hückel (DH) equations, except that the charge and salt sources due to mobile ions are replaced by their local values according to the Boltzmann distribution. On the one hand, Eq. (11) is a Poisson-Boltzmann like equation where appears the local charge density proportional to $\sinh \phi_0$. This equation handles the asymmetry induced by the surface through the electrostatic potential ϕ_0 , which ensures electroneutrality. This asymmetry may be due to the effect of the surface charge on anion- and cation-distributions (see Section III B) or due to dielectric boundaries and image charges at neutral interfaces, which give rise to interactions proportional to q^2 , and induce a local non-zero ϕ_0 for asymmetric electrolytes (see Section III A). On the other hand, the generalized DH equation Eq. (12), where appears the local ionic concentration proportional to $\cosh \phi_0$, fixes the Green's function $v_0(\mathbf{r}, \mathbf{r}')$ evaluated at \mathbf{r} with the charge source located at \mathbf{r}' and takes into account dielectric jumps at boundaries.

These variational equations were first obtained within the variational method by Netz and Orland [19]. They were also derived in Ref. [31] within the Debye closure approach and the BBGKY hierarchic chain. Yaroshchuk obtained an approximate solution of the closure equations for confined electrolyte systems in order to study ion exclusion from membranes [6].

Equations (11)–(12) enclose the limiting cases of WC ($\Xi \rightarrow 0$) and SC ($\Xi \rightarrow \infty$). To see that, it is interesting to rewrite these equations by normalizing all lengths and the fixed charge density, $\rho_s(\mathbf{r})$, by the Gouy-Chapman length according to $\tilde{\mathbf{r}} = \mathbf{r}/\ell_G$, $\tilde{\rho}_s(\tilde{\mathbf{r}}) = \ell_G \rho_s(\mathbf{r})/\sigma_s$ (σ_s is the average surface charge density). By introducing a new electrostatic potential $\tilde{\phi}_0(\mathbf{r}) = q\phi_0(\mathbf{r})$, one can

express the same set of equations in an adimensional form

$$\tilde{\Delta}\tilde{\phi}_0(\tilde{\mathbf{r}}) - \Lambda e^{-\frac{\tilde{W}}{\Xi}(\tilde{\mathbf{r}})} \sinh \tilde{\phi}_0(\tilde{\mathbf{r}}) = -2\tilde{\rho}_s(\tilde{\mathbf{r}}) \quad (14)$$

$$\begin{aligned} -\tilde{\Delta}\tilde{v}_0(\tilde{\mathbf{r}}, \tilde{\mathbf{r}}') + \Lambda e^{-\frac{\tilde{W}}{\Xi}(\tilde{\mathbf{r}})} \cosh \tilde{\phi}_0(\tilde{\mathbf{r}})\tilde{v}_0(\tilde{\mathbf{r}}, \tilde{\mathbf{r}}') \\ = 4\pi\delta(\tilde{\mathbf{r}} - \tilde{\mathbf{r}}') \end{aligned} \quad (15)$$

where $\tilde{v}_0 = v_0\ell_G/\ell_B$, $\tilde{W} = W\ell_G/\ell_B$ and we have also introduced the rescaled fugacity $\Lambda = 8\pi\lambda\ell_G^3\Xi$ [32]. Now, one can check that, in both limits $\Xi \rightarrow 0$ and $\Xi \rightarrow \infty$, the coupling between ϕ_0 and v_0 in Eq. (11) disappears and the theory becomes integrable. Finally, it is important to note that this adimensional form of variational equations allows one to focus on the role of $v_0(\mathbf{r}, \mathbf{r}')$ whose strength is controlled by Ξ in Eqs. (14) and (15). However, even at the numerical level, their explicit coupling does not allow for exact solutions for general Ξ .

In the present work, we make a restricted choice for $v_0(\mathbf{r}, \mathbf{r}')$ and replace the local salt concentration in the form of a local Debye-Hückel parameter (or inverse screening length) $\kappa(\mathbf{r})$ in Eq. (12),

$$\kappa(\mathbf{r})^2 = 8\pi\ell_B q^2 \lambda e^{-\frac{q^2}{2}W(\mathbf{r})} \cosh [q\phi_0(\mathbf{r})], \quad (16)$$

by a constant piecewise one $\kappa_v(\mathbf{r}) = \kappa_v$ in the presence of ions and $\kappa_v(\mathbf{r}) = 0$ in the salt-free parts of the system. Note that it has been recently shown that many thermodynamic properties of electrolytes are successfully described with a Debye-Hückel kernel [33].

The inverse kernel (or the Green's function) $v_0(\mathbf{r}, \mathbf{r}')$ is then taken to be the solution to a generalized Debye-Hückel (DH) equation

$$[-\nabla(\epsilon(\mathbf{r})\nabla) + \epsilon(\mathbf{r})\kappa_v^2(\mathbf{r})] v_0(\mathbf{r}, \mathbf{r}') = \frac{e^2}{k_B T} \delta(\mathbf{r} - \mathbf{r}') \quad (17)$$

with the boundary conditions associated with the dielectric discontinuities of the system

$$\lim_{\mathbf{r} \rightarrow \Sigma^-} v_0(\mathbf{r}, \mathbf{r}') = \lim_{\mathbf{r} \rightarrow \Sigma^+} v_0(\mathbf{r}, \mathbf{r}'), \quad (18)$$

$$\lim_{\mathbf{r} \rightarrow \Sigma^-} \epsilon(\mathbf{r})\nabla v_0(\mathbf{r}, \mathbf{r}') = \lim_{\mathbf{r} \rightarrow \Sigma^+} \epsilon(\mathbf{r})\nabla v_0(\mathbf{r}, \mathbf{r}') \quad (19)$$

where Σ denotes the dielectric interfaces. We now restrict ourselves to planar geometries. We split the grand potential (9) into three parts, $F_v = F_1 + F_2 + F_3$, where F_1 is the mean electrostatic potential contribution,

$$\begin{aligned} F_1 = S \int dz \left\{ -\frac{[\nabla\phi_0(z)]^2}{8\pi\ell_B} + \rho_s(z)\phi_0(z) \right. \\ \left. - \sum_i \lambda_i e^{-\frac{q_i^2}{2}W(z) - q_i\phi_0(z)} \right\}, \end{aligned} \quad (20)$$

F_2 the kernel part and F_3 the unscreened Van der Waals contribution. The explicit forms of F_2 and F_3 are reported in Appendix A. The first variational equation is given by $\partial F_v/\partial\kappa_v = \partial(F_1 + F_2)/\partial\kappa_v = 0$. This equation is the restricted case of Eq. (12). As we will see

below, its explicit form depends on the confinement geometry of the electrolyte system as well as on the form of $\epsilon(\mathbf{r})$. The variational equation for the electrostatic potential [34] $\delta F_v/\delta\phi_0(z) = 0$ yields regardless of the confinement geometry

$$\frac{\partial^2\phi_0}{\partial z^2} + 4\pi\ell_B\rho_s(z) + \sum_i 4\pi\ell_B q_i \lambda_i e^{-\frac{q_i^2}{2}W(z) - q_i\phi_0(z)} = 0. \quad (21)$$

The second-order differential equation (21), which is simply the generalization of Eq. (11) for a general electrolyte in a planar geometry, does not have closed-form solutions for spatially variable $W(z)$. In what follows, we optimize the variational grand potential F_v using restricted forms for the electrostatic potential $\phi_0(z)$ and compare the result to the numerical solution of Eq. (21) for single interfaces and slit-like pores.

The single ion concentration is given by

$$\rho_i(z) = \lambda_i e^{-\frac{q_i^2}{2}W(z) - q_i\phi_0(z)} \quad (22)$$

and its spatial integral by

$$\int dz \rho_i(z) = -\lambda_i \frac{\partial F_v}{\partial \lambda_i}. \quad (23)$$

We define the Potential of Mean Force (PMF) of ions of type i , $\Phi_i(z)$, as

$$\Phi_i(z) \equiv -\ln \frac{\rho_i(z)}{\rho_b} \quad (24)$$

By defining

$$w(z) \equiv W(z) - W_b \quad (25)$$

where W_b is the value of $W(z)$ in the bulk and comparing Eqs. (22)–(24), we find

$$\Phi_i(z) = \frac{q_i^2}{2}w(z) + q_i\phi_0(z) \quad (26)$$

$$\frac{q_i^2}{2}W_b = \ln \gamma_i^b \equiv \mu_i - \ln(\rho_b \lambda_i^3) \quad (27)$$

Hence, $q_i^2 W_b/2$ is nothing else but the excess chemical potential of ion i in the bulk and $q_i^2 W(z)/2 = \ln \gamma_i(z)$ is its generalization for ion i at distance z from the interface. They are related to the activity coefficients γ_i^b and $\gamma_i(z)$. Note that the zero of the chemical potential is fixed by the condition that ϕ_0 vanishes in the bulk. The PMF, Eq. (26), is thus the mean free energy per ion (or chemical potential) needed to bring an ion from the bulk at infinity to the point at distance z from the interface, taking into account correlations with the surrounding ionic cloud.

Before applying the variational procedure to single and double interfaces, let us consider the variational approach in the bulk. In this case, the variational potential ϕ_0 is

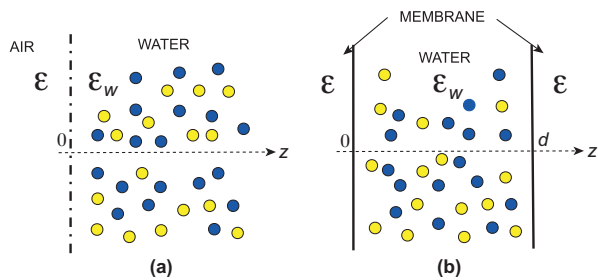


FIG. 1: (color online) Geometry for a single dielectric interface (e.g. water–air) (a) and double interfaces or slit-like pores (b).

equal to 0, and the variational grand potential F_v only depends on κ_v . Two minima appear: one metastable minimum κ_v^0 at low values of κ_v , and a global minimum at infinity ($F_v \rightarrow -\infty$ for $\kappa_v \rightarrow \infty$) which is unphysical since at these large concentration values, finite size effects should be taken into account. It has been shown by introducing a cutoff at small distances [20], that, for physical temperatures, this instability disappears and the global minimum of F_v is $\kappa_v^0 \approx \kappa_b$ given by the Debye–Hückel limiting law:

$$\begin{cases} \mu_i = \ln(\rho_b \lambda_i^3) - \frac{q_i^2}{2} \kappa_b \ell_B \\ \kappa_b^2 = 4\pi \ell_B \sum_i q_i^2 \rho_{i,b} \end{cases} \quad (28)$$

From Eq. (27), we thus find $W_b \approx -\kappa_b \ell_B$ and the potential $w(z)$ reduces to

$$w(z) \approx v_0(z, z) - v_c^b(0) + \kappa_b \ell_B, \quad (29)$$

which will be adopted in the rest of the paper. Furthermore, problems due to the formation of ion pairs do not enter at the level of the variational approach we have adopted. Let us also report the following conversion relations

$$\begin{aligned} I_b &\simeq 0.19(\kappa_b \ell_B)^2 \text{ mol.L}^{-1} \\ \kappa_b &\simeq 3.29\sqrt{I} \text{ nm}^{-1}, \end{aligned} \quad (30)$$

where $I = 1/2 \sum_i q_i^2 \rho_{i,b}$ is the ionic strength expressed in mol.L^{-1} . Finally, the single-ion densities are given by

$$\rho_i(z) = \rho_{i,b} e^{-\frac{q_i^2}{2} w(z) - q_i \phi_0(z)}. \quad (31)$$

III. SINGLE INTERFACE

The single interfacial system considered in this Section consists of a planar interface separating a salt-free left half-space from a right half-space filled up with an electrolyte solution of different species (Fig. 1). In the general case, the dielectric permittivity of the two half spaces may be different (we note ϵ the permittivity in the salt-free part). The Green's function, which is chosen to be solution of the DH equation with $\epsilon(z) = \epsilon\theta(-z) + \epsilon_w\theta(z)$

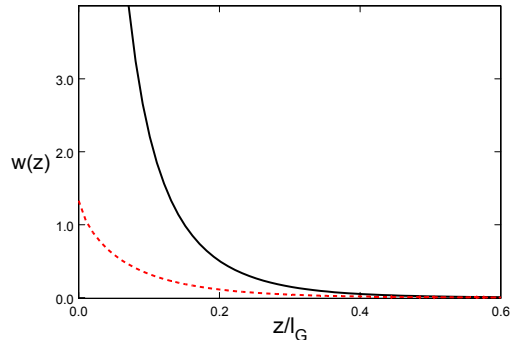


FIG. 2: (color online) Potential $w(z)$ in units of $k_B T$ for $\epsilon = 0$ (black solid curve), Eq. (36), and $\epsilon = \epsilon_w$ (red dashed curve) and $\kappa_b \ell_B = 4$.

and $\kappa(z) = \kappa_v \theta(z)$ where $\theta(z)$ stands for the Heaviside distribution, is given for $z > 0$ by [5]

$$w(z) = \ell_B(\kappa_b - \kappa_v) + \ell_B \int_0^\infty \frac{k dk}{\sqrt{k^2 + \kappa_v^2}} \Delta(k/\kappa_v) e^{-2\sqrt{k^2 + \kappa_v^2} z} \quad (32)$$

where

$$\Delta(x) = \frac{\epsilon_w \sqrt{x^2 + 1} - \epsilon x}{\epsilon_w \sqrt{x^2 + 1} + \epsilon x}. \quad (33)$$

and F_2 [Eq. (A4)] can be analytically computed [20]

$$F_2 = V \frac{\kappa_v^3}{24\pi} + S \Delta \frac{\kappa_v^2}{32\pi}, \quad (34)$$

where

$$\Delta \equiv \Delta(x \rightarrow \infty) = \frac{\epsilon_w - \epsilon}{\epsilon_w + \epsilon}. \quad (35)$$

The first term on the rhs. of Eq. (34) is simply the volumic Debye free energy associated with a hypothetical bulk with a Debye inverse screening length κ_v and the second term on the rhs. involves interfacial effects, including the dielectric jump Δ , and κ_v .

For the single interface system, as seen in Section II, F_3 is independent of κ_v and $\phi_0(z)$, which means that it does not contribute to the variational equations. By minimizing Eqs. (20) and (34) with respect to κ_v for fixed $\phi_0(\mathbf{r})$ and taking $V \rightarrow \infty$, one exactly find the same variational equation for κ_v as for the bulk case. Hence, as discussed above, we have $\kappa_v = \kappa_b$ given by Eq. (28) and the first term of the rhs. of Eq. (32) vanishes. This result was obtained in [20] for the special case $\phi(\mathbf{r}) = 0$. It is of course not surprising to end up with the same result for finite $\phi(\mathbf{r})$ since we know that the electrostatic potential should vanish in the bulk. This potential combines in an intricate way both the image charge and solvation contributions due to the presence of the interface. The image

force corresponds to the interaction of a given ion with the polarized charges at the interface and is equivalent to the interaction of the charged ion with its image located at the other side of the dielectric surface. As it is well known, the image charge interaction is repulsive for $\epsilon < \epsilon_w$ (e.g. water-air interface) and attractive for $\epsilon > \epsilon_w$ (the case for an electrolyte-metal interface) [35]. The interfacial reduction in solvation arises because an ion always prefers to be screened by other ions in order to reduce its free energy. Hence, it is attracted towards areas where the ion density is maximum (at least at not too high concentrations for which steric repulsion may predominate). This term is non-zero even for $\epsilon = \epsilon_w$ since for an ion close to the interface, there is a “hole” of screening ions in the salt-free region (where $\kappa_v = 0$). Although our choice of homogeneous variational inverse screening length allows us to handle the deformation of ionic atmospheres near interfaces that are impermeable to ions, it does not allow us to treat in detail the local variations in ion solvation free energy arising from ion-ion correlations (except in an average way in confined geometries where κ_v can differ from the bulk value of the inverse screening length, see Section IV below).

Equation (32) simplifies in three cases :

1) For $\epsilon = 0$ ($\Delta = 1$), where the solvation effect vanishes because the lines of forces are totally excluded from the air region [35], Eq. (32) reduces to

$$w(z) = \ell_B \frac{e^{-2\kappa_b z}}{2z}. \quad (36)$$

This is the case where the image charge repulsion is the strongest (see Fig. 2).

2) A slightly better approximation for $\epsilon \neq 0$ can be obtained by artificially allowing salt to be present in the air region. This gives rise to the “undistorted ionic atmosphere” approximation [6], for which $w(z)$ in Eq. (36) is multiplied by Δ :

$$w(z) = \Delta \ell_B \frac{e^{-2\kappa_b z}}{2z}. \quad (37)$$

Solvation effects are now absent and salt exclusion arises solely from dielectric repulsion. Eq. (37) is exact for arbitrary κ_b and $\Delta = 1$, or arbitrary Δ and $\kappa_b = 0$.

3) In the absence of a dielectric discontinuity $\epsilon = \epsilon_w$ ($\Delta = 0$), the potential can be expressed as

$$w(z) = \kappa_b \ell_B f(\kappa_b z) \quad (38)$$

$$f(x) = \frac{(1+x)^2 e^{-2x}}{2x^3} - \frac{K_2(2x)}{x}$$

where $K_2(x)$ is the Bessel function of the second kind. One notices that unlike the case $\Delta > 0$, the potential has a finite value at the interface, i.e. $w(0) = \kappa_b \ell_B / 3$.

We note that in this case of one interface, we have $\lim_{z \rightarrow \infty} \phi_0(z) = 0$ and the fugacity λ_i of each species is fixed by its bulk concentration according to

$$\rho_{i,b} = \lim_{z \rightarrow \infty} \rho_i(z) = \lambda_i e^{\frac{q_i^2}{2} \kappa_b \ell_B} \quad (39)$$

where we used Eq. (22).

A. Neutral dielectric interface

We investigate in this section the physics of an asymmetric electrolyte close to a neutral dielectric interface (e.g. water-air, liquid-liquid or liquid-solid interface) located at $z = 0$ ($\sigma_s = 0$). For the sake of simplicity, we assume $\epsilon = 0$, which is a very good approximation for the air-water interface characterized by $\epsilon = 1$ (see the discussion in Ref. [4]). Hence we keep the approximation $w(z) = w_0(z)$ given by Eq. (36). The electrolyte is composed of two species of bulk density ρ_+ and ρ_- and charge $(q_+e), -(q_-e)$ with $q_+ > q_-$. In order to satisfy the electroneutrality in the bulk, we impose $\rho_+ q_+ = \rho_- q_-$. According to Eq. (28), the bulk inverse screening length noted κ_b is given by

$$\kappa_b^2 = 4\pi \ell_B q_- \rho_- (q_- + q_+) \quad (40)$$

and the variational equation (21) for the electrostatic potential is a modified Poisson-Boltzmann equation

$$\frac{\partial^2 \phi_0}{\partial z^2} + 4\pi \ell_B \rho_{\text{ch}}(z) = 0 \quad (41)$$

with a local charge concentration

$$\rho_{\text{ch}}(z) = \rho_- q_- \left[e^{-\frac{q_+^2}{2} w(z) - q_+ \phi_0(z)} - e^{-\frac{q_-^2}{2} w(z) + q_- \phi_0(z)} \right]. \quad (42)$$

Equation (41) can not be solved analytically. Its numerical solution, obtained using a 4th order Runge-Kutta method, is plotted in Fig. 3(a) for asymmetric electrolytes with divalent and quadrivalent cations and the local charge density is plotted in Fig. 3(b).

Fig. 3 clearly shows that, very close to the dielectric interface for $z < a$, image charge repulsion expulses all ions (since $\rho_{\text{ch}}(z) \sim \exp(-1/z)$ has an essential singularity) and ϕ_0 is flat. For $z > a$, but still close to the interface, there is a layer where the electrostatic field is almost constant (ϕ_0 increases linearly), which is created by the charge separation of ions of different valency due to repulsive image interactions. The intensity of image forces increases with the square of ion valency and close to the interface, $\rho_{\text{ch}}(z) < 0$ since we assumed $q_+ > q_-$ (the case for MgI_2). To ensure electroneutrality, the local charge then becomes positive when we move away from the surface (Fig. 3(b)), and the electrostatic potential goes exponentially to zero with a typical relaxation constant κ_ϕ . Moreover, in Fig. 3(a) one observes that when the charge asymmetry increases, the electrostatic potential also increases. Knowing that for symmetric electrolytes, $\phi_0 = 0$, our results confirm that the charge asymmetry is the source of the electrostatic potential ϕ_0 . Fig. 3(b) is qualitatively similar to Fig. 1 of Bravina who had derived an integral solution of Eq. (41) by using an approximation valid for $\kappa_b \ell_B \ll 1$ [5]. In order to go further in the description of the interfacial distribution of ions, we look for a restricted variational function $\phi_0(z)$ which not only contains a small number of variational

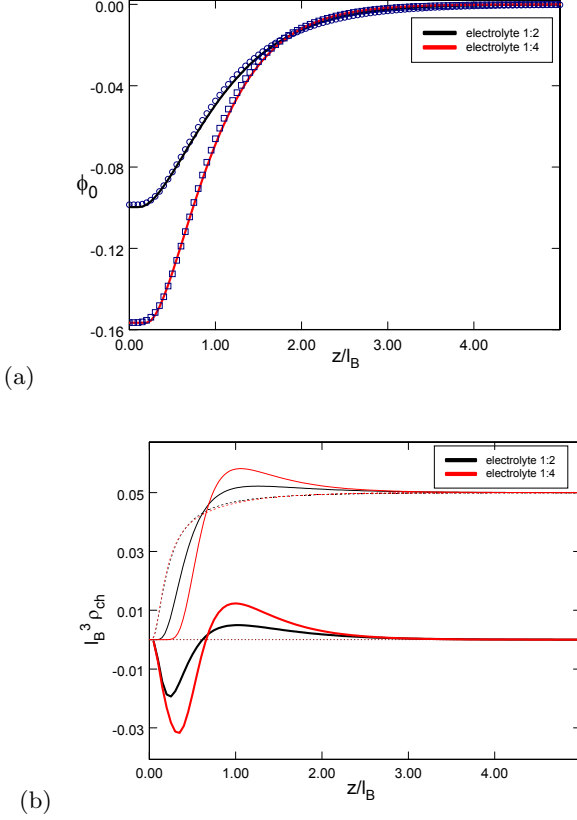


FIG. 3: (color online) (a) Electrostatic potential ϕ_0 (in $k_B T$ units) for asymmetric electrolytes: numerical solution of Eq. (41) (symbols) and variational choice, Eq. (44) (solid lines), for divalent and quadrivalent ions and $\rho_- = 0.242$ M. Variational parameters are $\kappa_\phi \simeq 1.4\kappa_b$, $a/l_B = 0.12; 0.21$ and $\varphi = -0.10; -0.156$. (b) Associated local charge density profile (thick lines) and anion (dashed lines) and cation (thin solid lines) concentrations.

parameters (such as a and κ_ϕ) but also is as close as possible to the numerical solution. As suggested by the description of Fig. 3, a continuous piecewise $\phi_0(z)$ is necessary to account for the essential singularity of $\rho_{\text{ch}}(z)$. To show this, let us expand Eq. (41) to order ϕ_0 :

$$\frac{\partial^2 \phi_0}{\partial z^2} \approx -4\pi\ell_B\rho_-q_- \left[e^{-\frac{q_+^2}{2}w(z)} - e^{-\frac{q_-^2}{2}w(z)} \right] + 4\pi\ell_B\rho_-q_- \left[q_+e^{-\frac{q_+^2}{2}w(z)} + q_-e^{-\frac{q_-^2}{2}w(z)} \right] \phi_0. \quad (43)$$

This linearization is legitimate, as seen in Fig. 3: $q_+|\phi_0(z)| < 1$ is satisfied for physical valencies. The first term in the rhs. of Eq. (43) corresponds to an effective local charge source while the second term is responsible for the screening of the potential. If we observe the charge distribution for $q^2w(z) > q\phi_0(z)$ and $z > a$, i.e. the first term of the rhs. of Eq. (43), we notice that it behaves like a distorted peak. The simplest function having a similar behavior is $f(z) = cz e^{-\kappa_\phi z}$, where c and κ_ϕ

are constants. Hence, we choose a restricted variational piecewise solution $\phi_0(z)$

$$\phi_0(z) = \begin{cases} \varphi & \text{for } z \leq a, \\ \varphi [1 + \kappa_\phi(z - a)] e^{-\kappa_\phi(z - a)} & \text{for } z \geq a. \end{cases} \quad (44)$$

whose derivation is explained in Appendix B. The variational parameters are the constant potential φ , the depletion distance a and the inverse screening length κ_ϕ . The grand potential (B5) derived for this solution was optimized with respect to the variational parameters using the Mathematica software. The restricted variational potential (44) is compared to the numerical solution of Eq. (41) in Fig. 3 for electrolytes 1 : 2 and 1 : 4 and $\rho_- \ell_B^3 = 0.05$. The agreement is excellent. One notices that the screening of the effective surface charge created by dielectric exclusion enters into play when $z > \kappa_\phi^{-1}$. Finally, let us note that since $\kappa_b l_B = 1.37$ and $\kappa_b l_B = 1.77$ respectively for the monovalent and quadrivalent electrolytes in Fig. 3, the method adopted by Bravina is not valid.

To summarize, the charge separation is taken into account by the potential φ (which increases with q_+/q_-) and the relaxation constant $\kappa_\phi \simeq 1.4\kappa_b$ is almost independent of q_+/q_- . Interestingly, the variational parameter $a/l_B \simeq 0.1 - 0.2$ is less than 1 nm. Indeed, for finite size ions, $w(z)$ differs from Eq. (36) very close to the interface and reaches a finite value at $z = 0$. The size of this region exactly corresponds to a which is of the order of an ion radius. This is thus an artifact of our point-like ion model and occurs only for asymmetric electrolytes at neutral surfaces.

The surface tension σ is equal to the excess grand potential defined as the difference between the grand potential of the interfacial system and that of the bulk system:

$$\sigma = \frac{\Delta\kappa_b^2}{32\pi} - \frac{\kappa_\phi\varphi^2}{32\pi\ell_B} - \rho_- \int_0^\infty dz \left\{ \left[e^{-\frac{q_-^2}{2}w(z) + q_- \phi_0(z)} - 1 \right] + \frac{q_-}{q_+} \left[e^{-\frac{q_+^2}{2}w(z) - q_+ \phi_0(z)} - 1 \right] \right\}. \quad (45)$$

The surface tension for electrolytes characterized by $q_- = 1$ and $q_+ = 1$ to 4 is plotted in Fig. 4 as a function of ρ_- , because the anion density is an experimentally accessible parameter. Unlike symmetric electrolytes [20], a plot with respect to κ_b^2 may lead to a different behavior. One notices that the increase in valency asymmetry leads to an important increase of the surface tension. This is of course mainly due to the reduction of the cation density in the bulk by a factor of q_-/q_+ necessary to satisfy the bulk electroneutrality (see the second term in the integral of Eq. (45)).

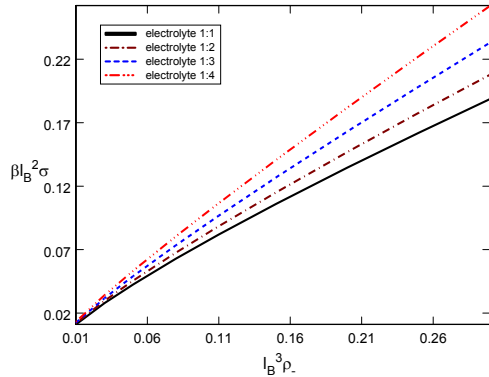


FIG. 4: (color online) Surface tension $\ell_B^2 \sigma / k_B T$ for asymmetric electrolytes vs. the anion bulk concentration, for increasing asymmetry $q_+ / q_- = 1$ to 4 from bottom to top.

B. Charged surfaces

We now consider a symmetric electrolyte in the proximity of an interface of constant surface charge $\sigma_s < 0$ located at $z = 0$. The variational equation (21) simplifies to

$$\frac{\partial^2 \tilde{\phi}_0}{\partial \tilde{z}^2} = 2\delta(\tilde{z}) + \tilde{\kappa}_b^2 e^{-\frac{\tilde{z}}{\tilde{h}}} \tilde{w}(\tilde{z}) \sinh \tilde{\phi}_0. \quad (46)$$

The mean-field limit ($\Xi \rightarrow 0$) of this equation corresponds to the NLPB equation, whose solution reads

$$\tilde{\phi}_0(\tilde{z}) = 4 \arctanh(\gamma_b e^{-\tilde{\kappa}_b \tilde{z}}) \quad (47)$$

where $\gamma_b = \tilde{\kappa}_b - \sqrt{1 + \tilde{\kappa}_b^2}$. In this Section, we show that a piecewise solution for the electrostatic potential similar to the one introduced in Section III A agrees very well with the numerical solution of Eq. (46). Inspired by the existence of a salt-free layer close to the interface and a mean-field regime far from the interface (WC), we propose two types of piecewise variational functions (see Appendix C). The first variational choice obeys the Poisson equation in the first zone of size h and the non-linear Poisson-Boltzmann solution in the second zone :

$$\tilde{\phi}_0^{\text{NL}}(\tilde{z}) = \begin{cases} 4 \arctanh \gamma + 2(\tilde{z} - \tilde{h}) & \text{for } \tilde{z} \leq \tilde{h}, \\ 4 \arctanh(\gamma e^{-\tilde{\kappa}_\phi(\tilde{z} - \tilde{h})}) & \text{for } \tilde{z} \geq \tilde{h}, \end{cases} \quad (48)$$

where $\gamma = \tilde{\kappa}_\phi - \sqrt{1 + \tilde{\kappa}_\phi^2}$. Variational parameters are h and an effective inverse screening length κ_ϕ . The second type of trial potential obeys the Laplace equation with a charge renormalization in the first zone and the linearized Poisson-Boltzmann solution in the second zone :

$$\tilde{\phi}_0^{\text{L}}(\tilde{z}) = \begin{cases} -\frac{2\eta}{\tilde{\kappa}_\phi} + 2\eta(\tilde{z} - \tilde{h}) & \text{for } \tilde{z} \leq \tilde{h}, \\ -\frac{2\eta}{\tilde{\kappa}_\phi} e^{-\tilde{\kappa}_\phi(\tilde{z} - \tilde{h})} & \text{for } \tilde{z} \geq \tilde{h}. \end{cases} \quad (49)$$

Variational parameters are \tilde{h} , $\tilde{\kappa}_\phi$, and the charge renormalization η , which takes into account the non-linear effects at the mean-field level [19]. The explicit form of the

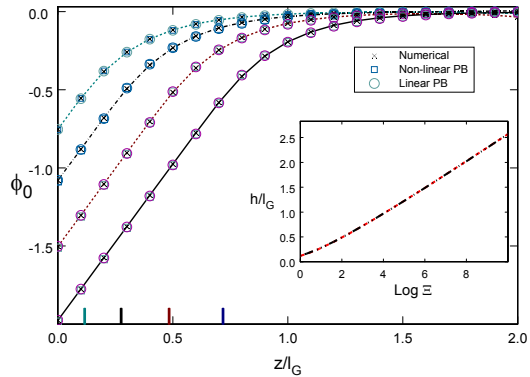


FIG. 5: (color online) Electrostatic potential, ϕ_0 (in units of $k_B T$): numerical solution of Eq. (46) (symbols) and restricted variational choices Eqs. (48) and (49) for $\epsilon = 0$, $\kappa_b \ell_G = 4$, and $\Xi = 1, 10, 100$, and 1000 (from top to bottom). The variational parameters are respectively $\kappa_\phi = 3.83, 3.74, 3.69, 3.66$ and $\eta \simeq 1$. Markers on the x -axis denote, for each curve, the size, \tilde{h} , of the SC zone, plotted vs. $\ln \Xi$ in the Inset.

associated variational free energies are reported in Appendix C. The inset of Fig. 5 displays the size of the SC layer h against Ξ . Our approach predicts a logarithmic dependence $\tilde{h} \propto \ln \Xi$, the factor behind the logarithm being $\tilde{\kappa}_b^{-1}$ for $\tilde{\kappa}_b \gg 1$. The restricted choices for ϕ_0 are compared with the full numerical solution of Eq. (41) in the same figure for $\epsilon = 0$. We see that, as in the previous section, the numerical solution and the restricted ones match perfectly. Hence salt-exclusion effects are essentially carried by the parameter h . Furthermore, one notices that $\tilde{\phi}_0(\tilde{z})$ relaxes to zero between $\tilde{z} = \tilde{h}$ and $\tilde{z} = \tilde{h} + 2\tilde{\kappa}_\phi^{-1}$. At $\kappa_b \ell_G = 4$ we are in the linear regime of the PB equation and therefore one has $\eta \simeq 1$. The charge renormalization idea was introduced by Alexander *et al.* [14], who showed that the non-linearity of the PB equation can be effectively taken into account at long distances by renormalizing the fixed charge source and extending the linearized zone where $|\tilde{\phi}_0| < 1$ to the whole domain. A linear solution of the form Eq. (49) can be very helpful for complicated geometries or in the presence of a non-uniform charge distribution where the NLPB equation does not present an analytical solution even at the mean-field level. These issues will be discussed in a future work.

Figure 6 displays the ion concentrations $\rho_i(z) / \rho_{i,b} = e^{-\Phi_i}$, which are related to the ion PMF Eq. (24), computed with the restricted solution Eq. (48) for several values of Ξ . As already said in the Introduction, in rescaled distance, the coupling parameter Ξ measures the strength of the excess chemical potential, $w(z)$. We first see that for coions as well as for counterions, the depletion layer in rescaled units in the proximity of the dielectric interface increases with Ξ due to the image charge repulsion and/or solvation effect, i.e. the term $e^{-\frac{\tilde{z}}{\tilde{h}}} \tilde{w}(\tilde{z})$ in Eq. (46). Furthermore, one notices that the counterion density ex-

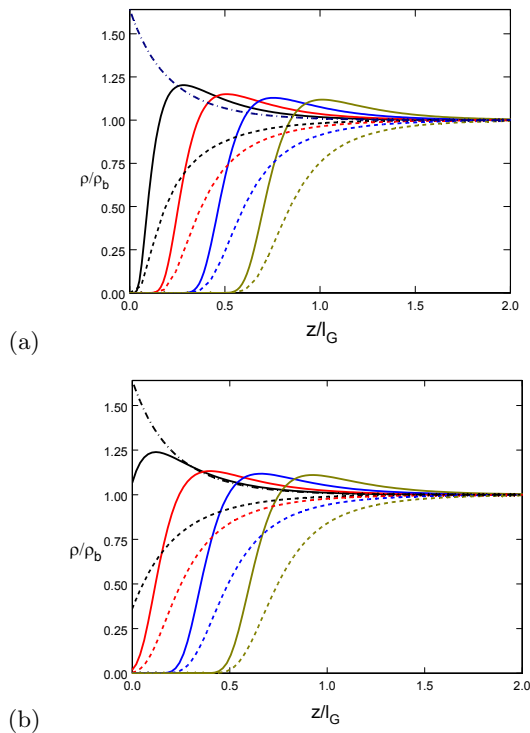


FIG. 6: (color online) Ion densities for $\kappa_b \ell_G = 4$, and (a) $\epsilon = 0$ and (b) $\epsilon = \epsilon_w$, for increasing coupling parameter: from left to right, $\Xi = 1, 10, 100$, and 1000 . Solid lines correspond to counterions, dashed lines to coions and dashed-dotted lines to the Poisson-Boltzmann result (47).

hibits a maximum. This concentration peak is due to the competition between the attractive force towards the charged wall and the repulsive image and solvation interactions. It is important to note that in the particular case $\epsilon = \epsilon_w$, there is no depletion layer for $\Xi < 10$.

IV. DOUBLE INTERFACE

In this Section, the variational method is applied to a double interface system which consists of a slit-like pore of thickness d , in contact with an external ion reservoir at its extremities (Fig. 1). The dielectric constant is ϵ_w inside the pore and ϵ in the outer space. The electrolyte occupies the pore and the external space is salt-free. The solution of the DH equation (A2) in this geometry is [6]

$$\begin{aligned}
 w(z) &= (\kappa_b - \kappa_v) \ell_B \\
 &+ \ell_B \int_0^\infty \frac{k dk}{\sqrt{k^2 + \kappa_v^2}} \frac{\Delta(k/\kappa_v)}{e^{2d\sqrt{k^2 + \kappa_v^2}} - \Delta^2(k/\kappa_v)} \\
 &\times \left[2\Delta(k/\kappa_v) + e^{2(d-z)\sqrt{k^2 + \kappa_v^2}} + e^{2z\sqrt{k^2 + \kappa_v^2}} \right]
 \end{aligned} \quad (50)$$

where $\Delta(x)$ is given in Eq. (33). The variational parameter of the Green's function is the variational inverse screening length κ_v which is taken uniform (generalized

Onsager-Samaras approximation, see [6, 21]). A more complicated approach has been previously developed in Ref. [21] where the authors introduced a piecewise form for the variational screening length, i.e. $\kappa(z) = \kappa_v$ over a layer of size h and $\kappa_v = \kappa_b$ in the middle of the pore. Although this choice is more general than ours, the minimization procedure with respect to κ_v is significantly longer than in our case and the variational equation is much more complicated. Consequently, this piecewise approach is not very practical when one wishes to study a charged membrane where the external field created by the surface charge considerably complicates the technical task (see Section IV B). We show that the simple variational choice adopted here captures the essential physics with less computational effort.

As in Eq. (32), the integral on the rhs. of Eq. (50) takes into account both image charge and solvation effects due to the two interfaces, whereas the first term is the Debye result for the difference between the bulk and a hypothetic bulk of inverse screening length κ_v . We should emphasize that, in the present case, the spatial integrations in Eqs. (A3)-(A4) run over the confined space, that is from $z = 0$ to $z = d$. By substituting the solution Eq. (50) into Eqs. (20)-(A5) and performing the integration over z , one finds [22]

$$\begin{aligned}
 \frac{F_2 + F_3}{S} &= \frac{d\kappa_v^3}{24\pi} + \frac{\Delta\kappa_v^2}{16\pi} \\
 &+ \frac{\kappa_v^2}{4\pi} \int_1^\infty dx x \ln [1 - \bar{\Delta}^2(x) e^{-2\kappa_v dx}] \\
 &+ \frac{\kappa_v^2}{8\pi} \int_1^\infty dx \frac{(\bar{\Delta}(x) - \bar{\Delta}^3(x)) / x - 2\kappa_v d \bar{\Delta}^2(x)}{e^{2d\kappa_v x} - \bar{\Delta}^2(x)}
 \end{aligned} \quad (51)$$

where we have defined $\bar{\Delta}(x) = \Delta(\sqrt{x^2 - 1})$.

The limiting case $\epsilon = 0$ allows for closed-form expressions. This limit is a good approximation for describing biological and artificial pores characterized by an external dielectric constant much lower than the internal one. In the following part of the work, we will deal most of the time with the special case $\epsilon = 0$, unless stated otherwise. In this limit, Eq. (51) simplifies to

$$\begin{aligned}
 \frac{F_2 + F_3}{S} &= \frac{\kappa_v^3 d}{24\pi} + \frac{\kappa_v^2}{16\pi} [1 + 2 \ln(1 - e^{-2d\kappa_v})] \\
 &- \frac{\kappa_v}{8\pi d} \text{Li}_2(e^{-2d\kappa_v}) - \frac{\text{Li}_3(e^{-2d\kappa_v})}{16\pi d^2}
 \end{aligned} \quad (52)$$

where $\text{Li}_n(x)$ stands for the polylogarithm function and $\xi(x)$ the Riemann zeta function (see Appendix D). Within the same limit ($\epsilon = 0$), $\Delta(x) = 1$ and we obtain an analytical expression for the Green's function Eq. (50)

$$\begin{aligned}
 w_0(z) &= (\kappa_b - \kappa_v) \ell_B - \frac{\ell_B}{d} \ln(1 - e^{-2d\kappa_v}) \\
 &+ \frac{\ell_B}{2d} \left[\beta \left(e^{-2d\kappa_v}; 1 - \frac{z}{d}, 0 \right) \right. \\
 &\left. + \frac{d}{z} e^{-2\kappa_v z} {}_2F_1 \left(1, \frac{z}{d}, 1 + \frac{z}{d}, e^{-2d\kappa_v} \right) \right]
 \end{aligned} \quad (53)$$

where $\beta(x; y, z)$ is the incomplete Beta function and ${}_2F_1(a, b; c; d)$ the hypergeometric series. The definitions of these special functions are given in Appendix D. At this step, the PMF thus depends on three adimensional parameters, namely $d\kappa_v$, $d\kappa_b$, and d/ℓ_B .

For the system with a single interface, the ion fugacity λ_i was fixed by the bulk density. In the present case where the confined system is in contact with an external reservoir, λ_i is fixed by chemical equilibrium:

$$\lambda_i = \lambda_{i,b} = \rho_{i,b} e^{-\frac{q_i^2}{2} \kappa_{i,b} \ell_B}, \quad (54)$$

where κ_b and $\lambda_{i,b}$ are respectively the inverse Debye screening length and the fugacity in the bulk reservoir [see Eq. (28)]. Once this constraint is taken into account, the last term of electrostatic part of the variational grand potential Eq. (20) can be written as

$$-\sum_i \rho_{i,b} \int_0^d dz e^{-\frac{q_i^2}{2} w(z) - q_i \phi_0(z)}. \quad (55)$$

Eq. (21) then becomes for a symmetric $q : q$ electrolyte:

The optimization of $F_v = F_1 + F_2 + F_3$ given by Eq. (20) and (52) with respect to the inverse trial screening length κ_v leads to the following variational equation for κ_v :

$$(d\kappa_v)^2 + d\kappa_v \tanh(d\kappa_v) = (d\kappa_b)^2 \int_0^1 dx e^{-\frac{q^2}{2} w_0(xd)} \times \cosh[\tilde{\phi}_0(xd)] \left\{ 1 + \frac{\cosh[(2x-1)d\kappa_v]}{\cosh(d\kappa_v)} \right\}. \quad (56)$$

Within the particular choice that fixed the functional form of the κ_v dependent Green's function Eq. (53), the two coupled equations (55) and (56) are the most general variational equations. In the following, we first consider the case of neutral pores and then the more general case of charged pores.

A. Neutral pore, symmetric electrolyte

In the case of a symmetric $q : q$ electrolyte and a neutral membrane, $\sigma_s = 0$, the solution of Eq. (55) is naturally $\phi_0 = 0$. The variational parameter κ_v is solution of Eq. (56) with $\phi_0 = 0$ and $w(z) = w_0(z)$ given by Eq. (53) when $\epsilon = 0$, which can be written as $d\kappa_v = f(d\kappa_b, \ell_B/d)$. Let us note that Eq. (56) can be solved with the Mathematica software in a fraction of a second.

Within the Debye-Hückel closure approach, Yaroshchuk (see Eq. (59) of Ref. [6]) obtains a self-consistent approximation for constant κ_v by replacing the exponential term of Eq. (12) with its average value in the pore:

$$\kappa_v^2 = \kappa_b^2 \int_0^1 dx e^{-\frac{q^2}{2} w(xd)}, \quad (57)$$

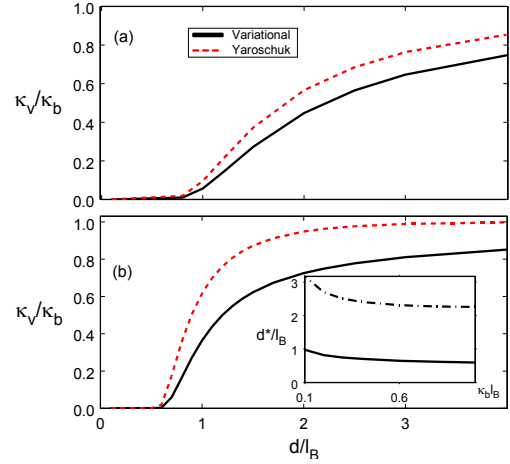


FIG. 7: (color online) Inverse screening length inside the neutral membrane (monovalent ions) normalized by κ_b vs. the pore size d/ℓ_B for $\epsilon = 0$ and (a) $\kappa_b \ell_B = 0.1$ ($\rho_b = 1.926$ mM), (b) $\kappa_b \ell_B = 1$ ($\rho_b = 0.1926$ M). Dashed lines correspond to the mid-point approximation, Eq. (58). The inset shows the characteristic pore size corresponding to total ionic exclusion as a function of the inverse bulk screening length. The bottom curve corresponds to monovalent ions and the top curve to divalent ions.

which should be compared with Eq. (56) with $\phi_0 = 0$. In order to simplify the numerical task, Yaroshchuk introduces a further approximation in which he replaces the potential $w(z)$ inside the depletion term of Eq. (57) by its value in the middle of the pore, $w(d/2)$. Then Eq. (57) takes the simpler form

$$\kappa_v^2 = \kappa_b^2 e^{-\frac{q^2}{2} w(d/2)}. \quad (58)$$

The self-consistent midpoint approximation is frequently used in nanofiltration theories [6, 28, 36]. For $\epsilon = 0$, the mid-point potential has the simple form $w(d/2) = (\kappa_b - \kappa_v)\ell_B - 2\ell_B \ln(1 - e^{-\kappa_v d})/d$. This approach is compared with the full variational treatment in Fig. 7 where the adimensional inverse screening length in the pore κ_v/κ_b is plotted as a function of the pore size d . We first note that as d decreases below a critical value d^* , the pore is empty of salt and $\kappa_v = 0$. The inset of Fig. 7 shows d^* versus the inverse bulk screening length. Searching for d such that $\kappa_v = 0$ in Eq. (56) leads to the same equation as Eq. (57), thus the value of d^* is identical within both approaches. However, Fig. 7 shows that the mid-point approximation, Eq. (58), overestimates the internal salt concentration as well as the abruptness of the crossover to an ion-free regime for decreasing pore size. Indeed, this approximation is equivalent to neglecting the strong ion exclusion close to the pore surfaces (which is larger than in the middle of the pore). A similar behavior was also observed in Fig. 6 of Ref. [21] for the screening length in the neighborhood of the dielectric interface.

The effect of the dielectric discontinuity is illustrated in Fig. 8(a) where the inverse internal screening length is

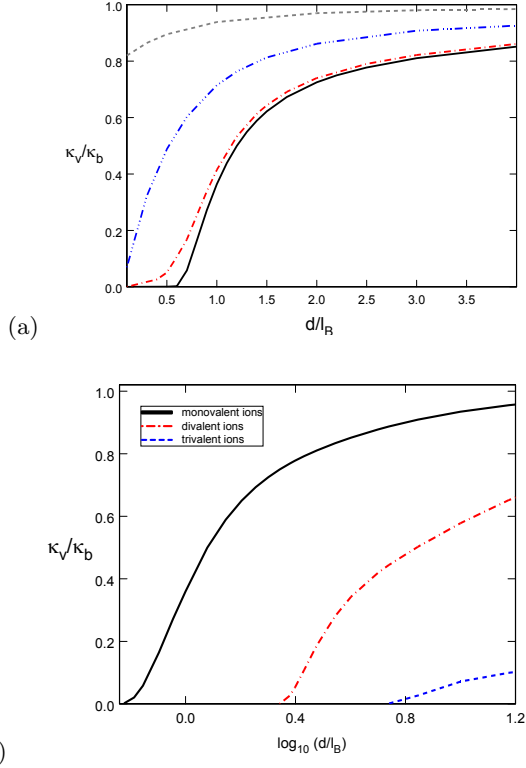


FIG. 8: (color online) Inverse screening length inside the membrane vs. the pore size d/ℓ_B ($\epsilon_w = 78$, $\kappa_b \ell_B = 1$). (a) From bottom to top: $\epsilon = 0$ ($\Delta = 1$), $\epsilon = 3.2$ ($\Delta = 0.92$), $\epsilon = 39$ ($\Delta = 1/3$), and $\epsilon = 78$ ($\Delta = 0$). (b) Log-linear plot for monovalent, divalent and trivalent ions, from left to right ($\epsilon = 0$).

compared for ϵ between 0 and $\epsilon_w = 78$ where the image-charge repulsion is absent and the solvation effect is solely responsible for ion repulsion. First of all, one observes that the total exclusion of ions in small pores is specific to the case $\epsilon = 0$. Moreover, in the solvation only case, the inverse screening length inside the pore only slightly deviates from the bulk value, $0.8 \leq \kappa_v/\kappa_b \leq 1$. This clearly indicates that, within the point-like ion model considered in this work, the image-charge interaction brings the main contribution to salt-rejection from neutral membranes. Roughly speaking, the image-charge and solvation effects come into play when the surface of the ionic cloud of radius κ_b^{-1} around a single ion located at the pore center touches the pore wall, i.e. for $\kappa_b^{-1} > d/2$. This simple picture fixes a characteristic length $d_{ch} \simeq 2\kappa_b^{-1}$ below which the internal ion density significantly deviates from the bulk value and ion-rejection takes place. This can be verified for intermediate salt densities in the bottom plot of Fig. 7 and the top plot of Fig. 8.

Since image-charge effects are proportional to q^2 , we illustrate in Fig. 8(b) the effect of ion valency q . At pore size $d \simeq 2.5\ell_B \simeq 1.8$ nm, where the inverse internal screening length for monovalent ions is close to 80 %

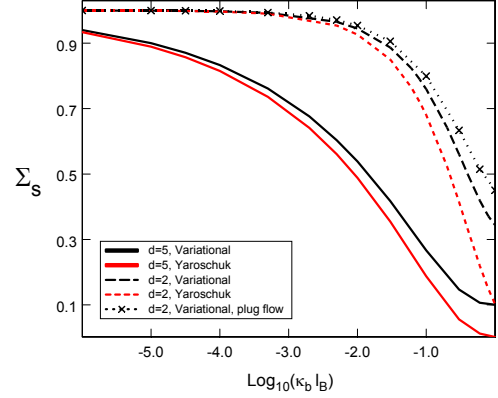


FIG. 9: (color online) Salt reflection coefficient (dimensionless) against the logarithm of the inverse bulk screening length for $\epsilon = 0$ and two pore sizes, $d/\ell_B = 2$ and 5 (red lines correspond to the mid-point approximation, Eq. (58)).

of its saturation value κ_b , the exclusion of divalent ions from the membrane is total. This effect driven by image interactions is even much more pronounced for trivalent ions. Since the typical pore size of nano-filtration membranes ranges between 0.5 and 2 nm, we thus explain why ion valency can play a central role in ion selectivity, even inside neutral pores.

The salt reflection coefficient, frequently used in membrane transport theories to characterize the maximum salt-rejection (obtained at high pressure) is related to the ratio of the net flux of ions across the membrane to that of the solvent volume flux J per unit transverse surface :

$$\begin{aligned} \Sigma_s &\equiv 1 - \frac{1}{J\rho_b} \int_0^d v_{||}(z)\rho(z)dz \\ &= 1 - 12 \int_{1/2}^1 x(1-x) e^{-\frac{q^2}{2}w(xd)} dx. \end{aligned} \quad (59)$$

where we have used, in the second equality, the Poiseuille velocity profile, $v_{||}(z) = \frac{6J}{d^3}z(d-z)$ in the pore and the PMF given by Eq. (24). It depends only on the parameters $\kappa_b \ell_B$ and d/ℓ_B . In certain nanopores with hydrophobic surfaces, the solvent flux may considerably deviate from the Poiseuille profile (see [37]). In this case, the velocity profile is flat, $v_{||}(z) = \frac{J}{d}$. We emphasize that since the velocity profile is normalized in both cases, the mid-point approximation is unable to distinguish between a Poiseuille and a plug flow velocity profile. Fig. 9 displays Σ_s as a function of the inverse bulk screening length for two pore sizes $d = 2\ell_B$ and $d = 5\ell_B$. As seen by Yaroshchuk, decreasing the pore size shifts the curves to higher bulk concentration and thus increases the range of bulk concentration where nearly total salt rejection occurs. However, quantitatively, the difference between the variational and mid-point approaches becomes significant at high bulk concentrations and this difference is accentuated in the case of plug-flow (for which Σ_s is higher

when compared to the Poiseuille case because the flow velocity no longer vanishes at the pore wall where the salt exclusion is strongest). This deviation is again due to the midpoint approximation of Eq. (58) in which the image interactions are underestimated. However since the velocity profile vanishes at the solid surface for the Poiseuille flow, the deficiencies of the mid-point approximation are less visible in Σ_s than in κ_v in this case.

Finally, we compute the disjoining pressure within our variational approach. We compare in Appendix E the result with that of the more involved variational scheme presented in Ref. [21] and show that one gets a very similar behaviour, revealing that the simpler variational method is able to capture the essential physics of the slit pore.

As stressed above, the main benefit obtained from the simpler approach proposed in this work is that the minimization procedure is much less time consuming. This point becomes crucial when considering the fixed charge of the membrane, which is thoroughly studied in the next section.

B. Charged pore, symmetric electrolyte

In this section, we apply the variational approach to a slit-like pore of surface charge $\sigma_s < 0$. In the following, we will solve Eqs. (55) and (56) numerically in order to test, as in the case of a single charged surface, the validity of restricted trial forms for $\phi_0(z)$. We define the partition coefficients in the pore for counterions and coions, k_+ and k_- , as

$$k_{\pm} \equiv \frac{\rho_{\pm}}{\rho_b} = \int_0^d \frac{dz}{d} e^{-\Phi_{\pm}(z)}. \quad (60)$$

where $\Phi_{\pm}(z)$ is given by Eq. (26).

1. Effective Donnan Potential

When one considers a charged nanopore, because of its small size, gradients of the potential ϕ_0 can be neglected as a first approximation. We thus assume a constant potential $\bar{\phi}_0$. The so-called effective *Donnan potential* $\bar{\phi}_0$ introduced by Yaroshchuk [6] will be fixed by the variational principle. By differentiating the grand potential Eq. (20) with respect to $\bar{\phi}_0$ (or equivalently integrating Eq. (55) from $z = 0$ to $z = d$ with $\nabla\bar{\phi}_0 = 0$), we find

$$2|\sigma_s| = -2q\rho_b \sinh(q\bar{\phi}_0) \int_0^d dz e^{-\frac{q^2}{2}w(z)} \quad (61)$$

which is simply the electroneutrality relation in the pore, taken in charge by the electrostatic potential $\bar{\phi}_0$. By

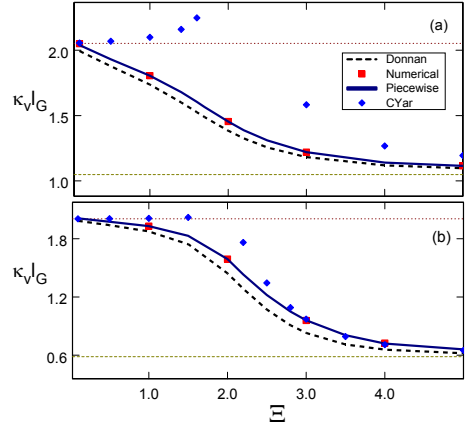


FIG. 10: (color online) Inverse internal screening length κ_v against Ξ for $\kappa_b \ell_G = 2$, $\epsilon = 0$ and (a) $d = 3\ell_G$ and (b) $d = 10\ell_G$. Comparison of various approximations: Yaroshchuk, Eq. (71) (diamonds), variational Donnan potential (dashed line), piecewise solutions (solid line), and numerical results (squares). Horizontal lines corresponds to the WC limit, Eq. (67) (top), and SC limit, Eq. (70) (bottom).

defining

$$\Gamma = \int_0^1 dx \exp[-q^2 \ell_B \bar{w}(xd)/(2d)] \quad (62)$$

$$= \int_0^1 dx \exp[-\Xi \bar{w}(x\tilde{d})/(2\tilde{d})], \quad (63)$$

where $\bar{w}(x) \equiv w(x)d/\ell_B$, we have $k_{\pm} = \Gamma \exp(\mp q\bar{\phi}_0)$ and Eq. (61) can be rewritten as

$$k_+ - k_- = 2 \frac{|\sigma_s|}{q\rho_b d} = \frac{X_m}{q\rho_b} = \frac{8}{\kappa_b^2 d \ell_G} = \frac{8}{\tilde{\kappa}_b^2 \tilde{d}} \quad (64)$$

where the second equality contains the Gouy-Chapman length ℓ_G and the quantity $X_m = 2|\sigma_s|/d$, frequently used in nanofiltration theories, corresponds to the volume charge density of the membrane. Hence, the partition coefficient of the charge, $k_+ - k_-$, does not depend on Ξ , i.e. charge image and solvation forces. By using Eq. (61) in order to eliminate the potential $\bar{\phi}_0$ from Eq. (60), one can rewrite the partition coefficients in the form

$$k_{\pm} = \Gamma e^{\mp q\bar{\phi}_0} = \sqrt{\Gamma^2 + \left(\frac{4}{\tilde{\kappa}_b^2 \tilde{d}}\right)^2} \pm \frac{4}{\tilde{\kappa}_b^2 \tilde{d}} \quad (65)$$

By substituting into Eq. (56) the analytical expression for $\bar{\phi}_0$ obtained from Eq. (61) (or Eq. (65)), one obtains a single variational equation for κ_v to be solved numerically,

$$(\tilde{d}\tilde{\kappa}_v)^2 + \tilde{d}\tilde{\kappa}_v \tanh(\tilde{d}\tilde{\kappa}_v) = (\tilde{d}\tilde{\kappa}_b)^2 \sqrt{\Gamma^2 + \left(\frac{4}{\tilde{\kappa}_b^2 \tilde{d}}\right)^2} \times \left\{ 1 + \int_0^1 dx e^{-\frac{\Xi}{2}\bar{w}(x\tilde{d})} \frac{\cosh\left[(2x-1)\tilde{d}\tilde{\kappa}_v\right]}{\Gamma \cosh(\tilde{d}\tilde{\kappa}_v)} \right\}. \quad (66)$$

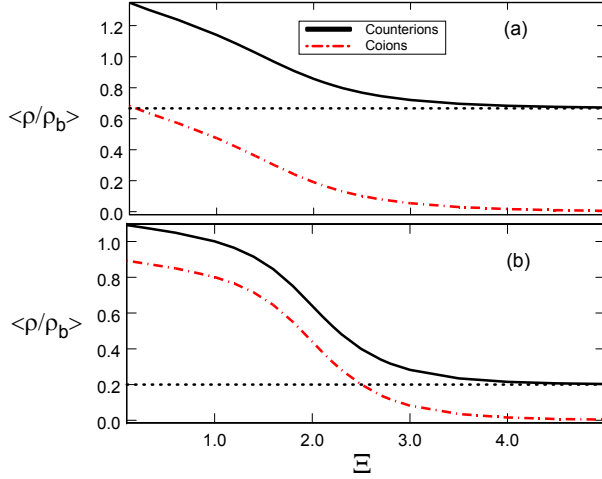


FIG. 11: (color online) Ionic partition coefficients, k_{\pm} , vs. Ξ for $\kappa_b \ell_G = 2$, $\epsilon = 0$, and (a) $d = 3\ell_G$ and (b) $d = 10\ell_G$. The horizontal line corresponds to the SC limit for counterions. As explained in the text, we note that $k_+ - k_- = 8/(\kappa_b^2 d \ell_G)$.

The numerical solution of Eq. (66) is plotted in Fig. 10 as a function of the coupling parameter Ξ . We see that as we move from the WC limit to the SC one by increasing Ξ , the pore evolves from a high to a low salt regime. This quite rapid crossover, which results from the exclusion of ions from the membrane, is mainly due to repulsive image-charge and solvation forces controlled by Γ whose effects increase with increasing Ξ .

In Fig. 11 are plotted the partition coefficients of counterions and coions, Eq. (60), as a function of Ξ . Here again, k_{\pm} decreases with increasing Ξ . Moreover, we clearly see that the rejection of coions from the membrane becomes total for $\Xi > 4$. In other words, even for intermediate coupling parameter values, we are in a counterion-only state. This is obviously related to the electrical repulsion of coions by the charged surface.

In the asymptotic WC limit ($\Xi \rightarrow 0$), $\Gamma = 1$ and we find the classical Donnan results in mean-field where $k_- = k_+^{-1} = e^{q\bar{\phi}_0}$ with $q\bar{\phi}_0 = \text{arcsinh}[4/(\tilde{\kappa}_b^2 \tilde{d})]$. The variational equations (66) and (65) reduce to

$$\kappa_v^2 = \kappa_b^2 \sqrt{1 + \left(\frac{4}{\tilde{\kappa}_b^2 \tilde{d}}\right)^2} \quad (67)$$

$$k_{\pm} = \sqrt{1 + \left(\frac{4}{\tilde{\kappa}_b^2 \tilde{d}}\right)^2} \pm \frac{4}{\tilde{\kappa}_b^2 \tilde{d}} \quad (68)$$

Quite interestingly, the relation Eq. (67) shows that, even in the mean-field limit, due to the ion charge imbalance created by the pore surface charge, the inverse screening length is larger than the Debye-Hückel value κ_b . In the case of small pores or strongly charged pores or at low values of the bulk ionic strength, i.e. $\kappa_b^2 \ell_G d \ll 1$ or $d\rho_b \ll |\sigma_s|/q$, we find $\kappa_v \simeq 2/\sqrt{\ell_G d}$ and $\rho_- = 0$ and $\rho_+ =$

$2|\sigma_s|/(dq)$. We thus find the classical Poisson-Boltzmann result for counterions only [24]. The counterion-only case is also called *good coion exclusion limit* (GCE), a notion introduced in the context of nanofiltration theories [6, 38, 39]. Hence, in this limit the quantity of counterions in the membrane is independent of the bulk density and depends only on the pore size d and the surface charge density σ_s . In the case of a membrane of size $d \simeq 1$ nm and fixed surface charge $\sigma_s \simeq 0.03$ nm $^{-2}$, this limit can be reached with an electrolyte of bulk concentration $\rho_b \simeq 50$ mM. In the opposite limit $\kappa_b^2 \ell_G d \gg 1$, one finds $\kappa_v \simeq \kappa_b$ and $\rho_{\pm} = \rho_b$.

In the SC limit $\Xi \rightarrow \infty$, $\Gamma = 0$ and Eq. (66) simplifies to

$$(\tilde{d}\tilde{\kappa}_v)^2 + \tilde{d}\tilde{\kappa}_v \tanh(\tilde{d}\tilde{\kappa}_v) = 4\tilde{d}[1 + \text{sech}(\tilde{d}\tilde{\kappa}_v)]. \quad (69)$$

For $d > \ell_G$ ($\tilde{d} > 1$), the solution of Eq. (69) yields with a high accuracy

$$\tilde{\kappa}_v \simeq \frac{\sqrt{1 + 16\tilde{d}} - 1}{2\tilde{d}}. \quad (70)$$

The partition coefficients simplify to $k_- = 0$ and $k_+ = 8/(\tilde{d}\tilde{\kappa}_b^2) = 2|\sigma_s|/(dq\rho_b)$ and we find the counterion only case (or GCE limit) without image charge forces discussed by Netz [24]. Partition coefficients in the SC limit and variational inverse screening length in both limits, Eqs. (67) and (70), are illustrated in Figs. 10 and 11 by dotted reference lines. Consequently, one reaches for $\Xi = 0$ the GCE limit exclusively for low salt density or small pore size, while the SC limit leads to GCE for arbitrary bulk density. It is also important to note that although the pore-averaged densities of ions are the same in the GCE limit of WC and SC regimes, the density profiles are different since when one moves away from the pore center, the counterion densities close to the interface increase in the WC limit due to the surface charge attraction and decrease in the SC limit due to the image charge repulsion.

It is interesting to compare this variational approach to the approximate mid-point approach of Yaroshchuk [6]. For charged membranes, he considers a constant potential and replaces the exponential term of Eqs. (11) and (12) by its value in the middle of the pore. He obtains the following self-consistent equations:

$$\kappa^2 = \kappa_b^2 e^{-\frac{q^2}{2}w(d/2)} \cosh(q\bar{\phi}_0) \quad (71)$$

$$2|\sigma_s| = -2qd\rho_b \sinh(q\bar{\phi}_0) e^{-\frac{q^2}{2}w(d/2)}. \quad (72)$$

The above set of equations are frequently used in nanofiltration theories [6, 28, 36]. By combining these equations in order to eliminate $\bar{\phi}_0$, one obtains an approximate non-linear equation for κ_v (approximation CYar in Fig. 10). In the limit of a high surface charge, the non-linear equations (71)–(72) depend only on the pore size d and the surface charge density σ_s :

$$\kappa^2 \simeq \frac{8\pi\ell_B q |\sigma_s|}{d} = \frac{4}{\ell_G d}. \quad (73)$$

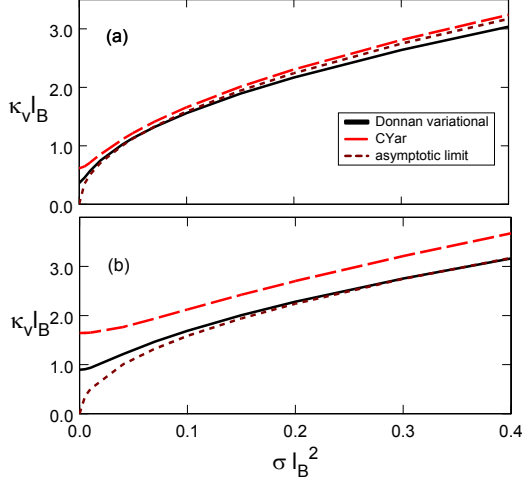


FIG. 12: (color online) Inverse internal screening length κ_v against the reduced surface charge $\bar{\sigma} = \ell_B^2 \sigma_s$ for $d = \ell_B$, $\epsilon = 0$ and (a) $\kappa_b \ell_B = 1$, (b) $\kappa_b \ell_B = 2$: constant variational Donnan approximation (solid line), asymptotic result Eq. (73) (dotted line) and Yaroshchuk approximation Eq. (71) (dashed line).

One can verify that in the regime of strong surface charge, Eq. (73) is also obtained from the asymptotic solution Eq. (70) since the dependence of the PMF on z is killed when $\Xi \rightarrow \infty$ and only the mid-pore value contributes. The numerical solution of Eq. (71)-(72) is illustrated as a function of Ξ in Fig. 10, and as a function of the surface charge in Fig. 12, together with the asymptotic formula Eq. (73). For the parameter range considered in Fig. 10, the solution of Eq. (71) strongly deviates from the result of the full variational calculation. For $\Xi < 2$, the mid-point approach follows an incorrect trend with increasing Ξ . It is clearly seen that at some values of the coupling parameter, Eqs. (71)-(72) do not even present a numerical solution. Using the relations $d/\ell_B = \tilde{d}/\Xi$ and $\ell_B \kappa_b = \Xi \tilde{\kappa}_b$ for monovalent ions, one can verify that the regime where the important deviations take place corresponds to high ion concentrations. This is confirmed in Fig. 12: the error incurred by the approximate mid-point solution of Yaroshchuk increases with the electrolyte concentration.

In Section IV A on neutral nanopores, it has been underlined that, due to the image charge repulsion, the ionic concentration inside the pore increases with the pore size d (see Fig. 8). In the present case of charged nanopores, this result is modified: Eqs. (67), (70) and (73) show that for strongly charged nanopores the concentration of ions inside the pore decreases with d . Moreover, the very high charge limit is a counterion-only state and Eq. (61) shows that, for a fixed surface charge density, electroneutrality alone fixes the number of counterions, N_- , in a layer of length d joining both interfaces, and image charge interactions play a little role. This is the reason why $\kappa_v^2 \propto \rho_- = N_-/(Sd)$ decreases for increasing d .

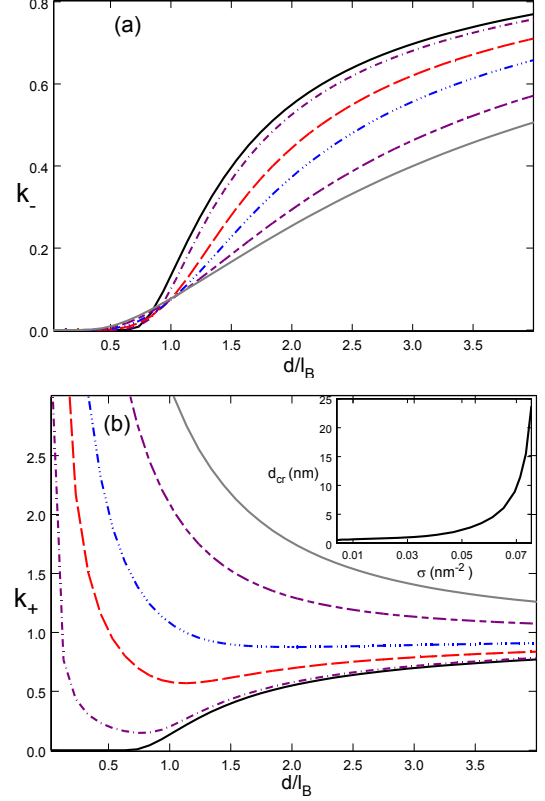


FIG. 13: (color online) Partition coefficient in the pore of coions (a) and counterions (b) vs. the pore size d/ℓ_B for increasing surface charge density, $\sigma_s \ell_B^2 = 0, 0.004, 0.02, 0.04, 0.08, 0.12$, from left to right, and $\kappa_b \ell_B = 1$. Inset: Critical pore size d_{cr} vs. the surface charge density σ_s ($\epsilon = 0$).

Hence, we expect an intermediate charge regime which interpolate between image force counterion repulsion (case of neutral pores, see Section IV A) and counterion attraction by the fixed surface charge. This is illustrated in Fig. 13 where the partition coefficients are plotted vs. d for increasing σ_s . As expected, coions are electrostatically pushed away by the surface charge which adds to the repulsive image forces, leading to a stronger coion exclusion than for neutral pores. The issue is more subtle for counterions: obviously, increasing the surface charge, σ_s , at constant pore size, d , increases k_+ . However, for small fixed σ_s , a regime where image charge and direct electrostatic forces compete, k_+ is non-monotonic with d . Below a characteristic pore size, $d < d_{cr}$, the electrostatic attraction dominates over image charge repulsion and due to the mechanism explained above, k_+ decreases for increasing d . For $d > d_{cr}$, the effect of the surface charge weakens and k_+ starts increasing with d . In this regime, the pore behaves like a neutral system. The inset of Fig. 13 shows that d_{cr} increases when σ_s increases. For highly charged membranes $\ell_B^2 \sigma_s \gg 0.1$, there is no minimum in $k_+(d)$, and the average counterion density in-

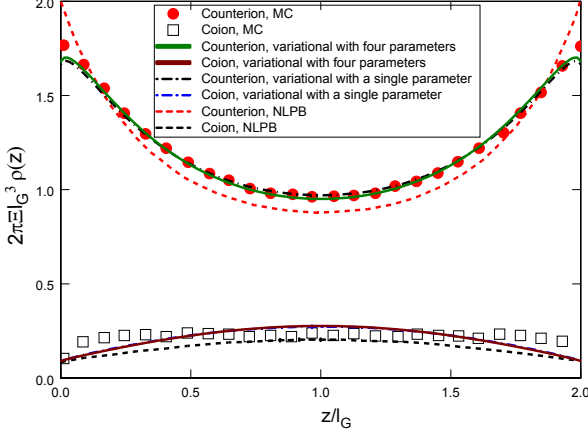


FIG. 14: (color online) Ion densities in the nanopore for $\epsilon = \epsilon_W$, $\Xi = 1$ and $h/l_G = 2$. The continuous lines correspond to the prediction of the variational method with four parameters, the dashed-dotted line the variational solution with a single parameter (see the text), the symbols are MC results (Fig. 2 of [29]) and the dashed lines denote the numerical solution of the non-linear PB result.

side the membrane monotonically decreases towards the bulk value. Experimental values for surface charges are $0 \leq \sigma_s \leq 0.5 \text{ nm}^{-2}$ (or $0 \leq \ell_B^2 \sigma_s \leq 0.25$), which corresponds to physically attainable values of d_{cr} . The interplay between image forces and direct electrostatic attraction is thus relevant to the experimental situation.

The variational Donnan potential approximation is thus of great interest since it yields physical insight into the exclusion mechanism and allows a reduction of the computational complexity. However, membranes and nanopores are often highly charged and spatial variations of the electrostatic potential inside the pore may play an important role. In the following we seek a piecewise solution for $\phi_0(z)$.

2. Piecewise solution

The variational modified PB equation (55) for $\tilde{\phi}_0$ shows that as one goes closer to the dielectric interface, $w(z)$ increases and the screening experienced by the potential $\tilde{\phi}_0$ gradually decreases because of ionic exclusion. This non-perturbative effect which originates from the strong charge-image repulsion inspires our choice for the variational potential $\tilde{\phi}_0(z)$. We opt for a piecewise solution as in Section III: a salt-free solution in the zone $0 < z < h$ and the solution of the linearized PB equation for $h < z < d/2$, with a charge renormalization parameter η taking into account non-linear effects. By inserting the boundary conditions $\partial\tilde{\phi}_0/\partial z|_{z=0} = 2\eta/\ell_G$ and $\partial\tilde{\phi}_0/\partial z|_{z=d/2} = 0$ and imposing the continuity of $\tilde{\phi}_0$ and its first derivative at $z = h$ [Eq. (B3)], the piecewise

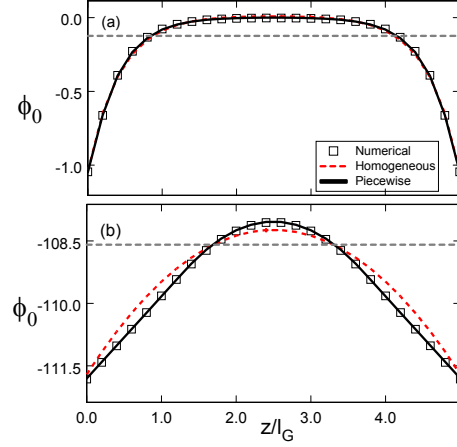


FIG. 15: (color online) Variational electrostatic potential (in units of $k_B T$) in the nanopore. Comparison of the numerical solution of Eq. (55) with the homogeneous ($h = 0$) and piecewise solution of Eq. (C5) for $\ell_G \kappa_b = 3$ and (a) $\Xi = 1$, (b) $\Xi = 100$. The horizontal line is the Donnan potential obtained from Eq. (61) ($\epsilon = 0$).

potential, solution of Eq. (55) with $\kappa_b^2 \exp[-q^2 w(z)/2]$ replaced by κ_ϕ^2 , takes the form

$$\tilde{\phi}_0(z) = \begin{cases} \bar{\varphi} - \frac{2\eta}{\ell_G} \left| z - \frac{d}{2} \right| & \text{for } 0 < z \leq h, \\ \varphi - \frac{2\eta}{\ell_G \kappa_\phi} \frac{\cosh[\kappa_\phi(d/2-z)]}{\sinh[\kappa_\phi(d/2-h)]} & \text{for } h \leq z \leq d/2 \end{cases} \quad (74)$$

where

$$\bar{\varphi} = \varphi + \frac{2\eta}{\ell_G} \left(\frac{d}{2} - h \right) - \frac{2\eta}{\ell_G \kappa_\phi} \coth \left[\kappa_\phi \left(\frac{d}{2} - h \right) \right] \quad (75)$$

is imposed by continuity, and κ_ϕ , φ , h and η are the variational parameters. By injecting the piecewise solution Eq. (C5) into Eq. (20), we finally obtain

$$\begin{aligned} \frac{F_1}{S} = & -\frac{2|\sigma_s|}{q} \left\{ \eta(\eta-2) \frac{h}{\ell_G} - \frac{\eta^2(d/2-h)}{2\ell_G \sinh^2[\kappa_\phi(d/2-h)]} \right. \\ & \left. + \frac{\eta(\eta-4)}{2\ell_G \kappa_\phi} \coth[\kappa_\phi(d/2-h)] + \varphi \right\} \\ & - \frac{\kappa_b^2}{4\pi\ell_B q^2} \int_0^d dz e^{-\frac{q^2}{2} w(z)} \cosh \tilde{\phi}_0(z). \end{aligned} \quad (76)$$

The solution to the variational problem is found by optimization of the total grand potential $F = F_1 + F_2$ with respect to κ_ϕ , φ , h , η and κ_v , where $F_2 + F_3$ is given by Eq. (52) for a general value of ϵ and by Eq. (52) for $\epsilon = 0$. This was easily carried out with Mathematica software.

A posteriori, we checked that two restricted forms for ϕ_0 , homogeneous with $h = 0$ and piecewise with $\varphi = 0$, were good variational choices. Fig. 14 compares the ion densities obtained from the variational approach with homogeneous ϕ_0 with the predictions of the MC simulations [29] and the NLPB equation for $\epsilon = \epsilon_W$, $\tilde{d} = 2$ and $\Xi = 1$. Two variational choices are displayed in this

figure, namely, the homogeneous approach with four parameters $\kappa_v = 1.68, \kappa_\phi = 1.36, \varphi = 0.16, \eta = 0.97$ and a simpler choice with $\eta = 1, \kappa_\phi = \kappa_v$ and two variational parameters: $\kappa_v = 1.69, \phi = -0.18$. In the latter case, one can obtain an analytical solution for φ and injecting this solution into the free energy, one is left with a single parameter κ_v to be varied in order to find the optimal solution. We notice that with both choices, the agreement between the variational method and MC result is good. It is clearly seen that the proposed approach can reproduce with a good quantitative accuracy the reduced solvation induced ionic exclusion, an effect absent at the mean-field level. Moreover, we verified that with the single parameter choice, one can reproduce at the mean-field variational level the ion density profiles obtained from the numerical solution of the NLPB equation (dashed lines in Fig. 14) almost exactly. We finally note that the small discrepancy between the predictions of the variational approach and the MC results close to the interface may be due to either numerical errors in the simulation, or our use of the generalized Onsager-Samaras approximation (our homogeneous choice for the inverse effective screening length appearing in the Green's function v_0 does not account for local enhancement or diminution of ionic screening due to variations in local ionic density).

For $\epsilon = 0$, the piecewise and homogeneous solutions are compared with the full numerical solution of Eqs. (55)–(56) in Fig. 15 for $\Xi = 1$ and 100. First of all, one observes that for $\Xi = 1$, both variational solutions match perfectly well with the numerical solutions. For $\Xi = 100$, the piecewise solution matches also perfectly well with the numerical one, whereas the matching of the homogeneous one is poorer. The optimal values of the variational parameters $(\kappa_v, \kappa_\phi, \eta, h)$ for the piecewise choice are $(2.57, 2.6, 0.98, 0.15)$ for $\Xi = 1$ and $(0.83, 0.13, 0.97, 1.37)$ for $\Xi = 100$.

The form of the electrostatic potential $\phi_0(z)$ is intimately related to ionic concentrations. Ion densities inside the pore are plotted in Fig. 16 for $\Xi = 1$ and $\Xi = 100$. We first notice that even at $\Xi = 1$, the counterion density is quite different from the mean-field prediction. Furthermore, due to image charge and electrostatic repulsions from both sides, the coion density has its maximum in the middle of the pore. On the other hand, the counterion density exhibits a double peak, symmetric with respect to the middle of the pore, which originates from the attractive force created by the fixed charge and the repulsive image forces. When Ξ increases, we see that the counterion density close to the wall shrinks and becomes practically flat in the middle of the pore. Hence the potential ϕ_0 linearly increases with z until the counterion-peak is reached and then it remains almost constant since the counterion layer screens the electrostatic field created by the surface charge (since in Fig. 15, z is renormalized by the Gouy-Chapman length which decreases with increasing σ_s , one does not see the increase of the slope $\phi_0(z=0)$). In agreement with the variational Donnan approximation above, coions are totally excluded from

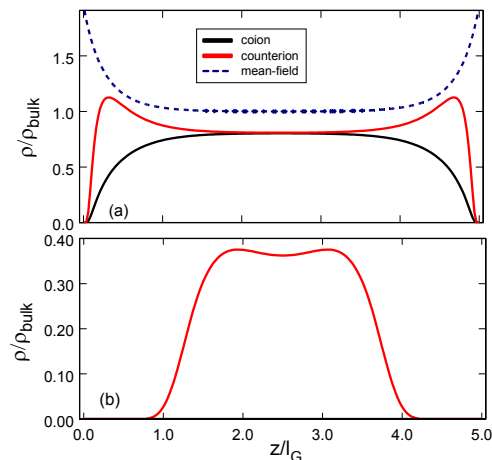


FIG. 16: (color online) Local ionic partition coefficient in the nanopore (same parameters as in Fig. 15 and $\epsilon = 0$) computed with the piecewise solution. (a) $\Xi = 1$, (b) $\Xi = 100$. The dotted line in the top plot corresponds to the mean-field prediction for counterion density.

the pore for large Ξ . Hence, the piecewise potential allows one to go beyond the variational Donnan approximation within which the density profile does not exhibit any concentration peak.

The inverse screening length κ_v obtained with the piecewise solution is compared in Fig. 10 with the prediction of the Donnan approximation and that of the numerical solution. The agreement between piecewise and numerical solutions is extremely good. Although the Donnan approximation slightly underestimates the salt density in the pore, its predictions follow the correct trend.

V. CONCLUSION

In this study, we applied the variational method to interacting point-like ions in the presence of dielectric discontinuities and charged boundaries. This approach interpolates between the WC limit ($\Xi \ll 1$) and the SC one ($\Xi \gg 1$), originally defined for charged boundaries without dielectric discontinuity, and takes into account image charge repulsion and solvation effects. The variational Green's function v_0 has a Debye-Hückel form with a variational parameter κ_v and the average variational electrostatic potential $\phi_0(z)$ is either computed numerically or a restricted form is chosen with variational parameters. The physical content of our restricted variational choices can be ascertained by inspecting the general variational equations (Eqs. (11)–(12) for symmetric salts). The generalized Onsager-Samaras approximation that we have adopted for the Green's function replaces a local spatially varying screening length by a constant variational one; although near a single interface this screening length is equal to the bulk one, in confined

geometries the constant variational screening length can account in an average way for the modified ionic environment (as compared with the external bulk with which the pore is in equilibrium) and can therefore strongly deviate from the bulk value. This modified ionic environment arises both from dielectric and reduced solvation effects present even near neutral surfaces (encoded in the Green's function) and the surface charge effects encoded in the average electrostatic potential. Our restricted variational choice for $\phi_0(z)$ is based on the usual non-linear Poisson-Boltzmann type solutions with a renormalized inverse screening length that may differ from the one used for v_0 and a renormalized external charge source. The coupling between v_0 and ϕ_0 arises because the inverse screening length for v_0 depends on ϕ_0 and vice-versa. The optimal choices are the ones that extremize the variational free energy.

In the first part of the work, we considered single interface systems. For asymmetric electrolytes at a single neutral interface, the potential $\phi_0(z)$ created by charge separation was numerically computed. It was satisfactorily compared to a restricted piecewise variational solution and both charge densities and surface tension are calculated in a simpler way than Bravina [5] and valid over a larger bulk concentration range. The variational approach was then applied to a single charged surface and it was shown that a piecewise solution, characterized by two zones, can accurately reproduce the correlations and non-linear effects embodied in the more general variational equation. The first zone of size h is governed by a salt-free regime, while the second region corresponds to an effective mean-field limit. The variational calculation predicts a relation between h and the surface charge of the form $h \propto (c + \ln|\sigma_s|)/|\sigma_s|$ where the parameter c depends on the temperature and ion valency.

In the second part, we dealt with a symmetric electrolyte confined between two dielectric interfaces and investigated the important problem of ion rejection from neutral and charged membranes. We illustrated the effects of ion valency and dielectric discontinuity on the ion rejection mechanism by focusing on ion partition and salt reflection coefficients. We computed within a variational Donnan potential approximation, the inverse internal screening length and ion partition coefficients, and showed that for $\Xi > 4$ one reaches the SC limit, where the partition coefficients are independent of the bulk concentration and depend only on the size and charge of the nanopore. This result has important experimental applications, since it indicates that complete filtration can be done at low bulk salt concentration and/or high surface charge. Furthermore, we showed that, due to image interactions, the quantity of salt allowed to penetrate inside a *neutral* nanopore increases with the pore-size. In the case of strongly charged membranes, this behavior is reversed for the whole physical range of pore size. We quantified the interplay between the image charge repulsion and the surface charge attraction for counterions and found that even in the presence of a weak surface charge, the

competition between them leads to a characteristic pore size d_{cr} below which the counterion partition coefficient rapidly decreases with increasing pore size. On the other hand, for nanopores of size larger than d_{cr} the system behaves like a neutral pore. Our variational calculation was compared to the Debye closure approach and the mid-point approximation used by Yaroshchuk [6]. The closure equations have no exact solution even at the numerical level. Our approach, based on restricted variational choices, shows significant deviations from Yaroshchuk's mid-point approach at high ion concentrations and small pore size. Finally, the introduction of a simple piecewise trial potential for ϕ_0 , which perfectly matches the numerical solutions of the variational equations, enabled us to go beyond the variational Donnan potential approximation and thus account for the concentration peaks in counterion densities. We computed ion densities in the pore and showed that for $\Xi > 4$, the exclusion of coions from the pore is total. We also compared the ionic density profiles obtained from the variational method with MC simulation results and showed that the agreement is quite good, which illustrates the accuracy of the variational approach in handling the correlation effects absent at the mean-field level.

The main goal in this work was first to connect two different fields in the chemical physics of ionic solutions focusing on complex interactions with surfaces: field-theoretic calculations and nanofiltration studies. Moreover, on the one hand, this variational method allows one to consider, in a non-perturbative way, correlations and non-linear effects; on the other hand the choice of one constant variational Debye-Hückel parameter is simple enough to reproduce previous results and to illuminate the mechanisms at play. This approach is also able to handle, in a very near future, more complicated geometries, such as cylindrical nanopores, or a non-uniform surface charge distribution.

The present variational scheme also neglects ion-size effects and gives rise to an instability of the free energy at extremely high salt concentration. Second order corrections to the variational method may be necessary in order to properly consider ionic correlations leading to pairing [40, 41] and to describe the physics of charged liquids at high valency, high concentrations or low temperatures. Introducing ion size will also allow us to introduce an effective dielectric permittivity ϵ_p for water confined in a nanopore intermediate between that of the membrane matrix and bulk water, leading naturally to a Born-self energy term that varies inversely with ion size and depends on the difference between $1/\epsilon_w$ and $1/\epsilon_p$ [42, 43]. Furthermore, the incorporation of the ion polarizability [44] will yield a more complete physical description of the behavior of large ions [45]. Charge inversion phenomena for planar and curved interfaces is another important phenomenon that we would like to consider in the future [46]. Note, however, that our study of asymmetric salts near neutral surfaces reveals a closely related phenomenon: the generation

of an effective non-zero surface charge due to the unequal ionic response to a neutral dielectric interface for asymmetric salts. A further point that possesses experimental relevance is the role played by surface charge inhomogeneity. Strong-coupling calculations show that an inhomogeneous surface charge distribution characterized by a vanishing average value gives rise to an attraction of ions towards the pore walls, but this effect disappears at the mean-field level [47]. For a better understanding of the limitations of the proposed model, more detailed comparison with MC/MD simulations are in order [48, 49]. Finally, dynamical hindered transport effects [27, 48] such as hydrodynamic forces deserve to be properly included in the theory for practical applications.

Acknowledgments

We would like to thank David S. Dean for numerous helpful discussions. This work was supported in part by the French ANR Program NANO-2007 (SIMO-NANOMEM project, ANR-07-NANO-055).

Appendix A: Variational free energy

For planar geometries (charged planes), the translational invariance parallel to the plane, allows us to significantly simplify the problem by introducing the partial Fourier-transformation of the trial potential in the form

$$v_0(z, z', \mathbf{r}_{||} - \mathbf{r}'_{||}) = \int \frac{d\mathbf{k}}{(2\pi)^2} e^{i\mathbf{k} \cdot (\mathbf{r}_{||} - \mathbf{r}'_{||})} \hat{v}_0(z, z', \mathbf{k}). \quad (\text{A1})$$

By injecting the Fourier decomposition (A1) into Eq. (17), the DH equation becomes

$$\left\{ -\frac{\partial}{\partial z} \epsilon(z) \frac{\partial}{\partial z} + \epsilon(z) [k^2 + \kappa_v^2(z)] \right\} \hat{v}_0(z, z', \mathbf{k}; \kappa_v(z)) = \frac{e^2}{k_B T} \delta(z - z'). \quad (\text{A2})$$

The translational symmetry of the system enables us to express any thermodynamic quantity in terms of the partially Fourier-transformed Green's function $\hat{v}_0(z, z, \mathbf{k})$. The average electrostatic potential contribution to F_v that follows from the average $\langle H \rangle_0$ reads

$$F_1 = S \int dz \left\{ -\frac{[\nabla \phi_0(z)]^2}{8\pi \ell_B} + \rho_s(z) \phi_0(z) - \sum_i \lambda_i e^{-\frac{q_i^2}{2} W(z) - q_i \phi_0(z)} \right\}, \quad (\text{A3})$$

the kernel part is

$$F_2 = \frac{S}{16\pi^2} \int_0^1 d\xi \int_0^\infty dk k \int dz \frac{\kappa_v^2(z)}{\ell_B(z)} \times \left[\hat{v}_0(z, z, \mathbf{k}; \kappa_v(z) \sqrt{\xi}) - \hat{v}_0(z, z, \mathbf{k}; \kappa_v(z)) \right] \quad (\text{A4})$$

where the first term in the integral follows from F_0 and the second term from $\langle H_0 \rangle_0$. Finally, the unscreened Van der Waals contribution, which comes from the unscreened part of F_0 , is given by

$$F_3 = \frac{S}{8\pi} \int_0^1 d\xi \int_0^\infty dz \left[\frac{1}{\ell_B(z)} - \frac{1}{\ell_B} \right] \langle (\nabla \phi)^2 \rangle_\xi - \ln \int \mathcal{D}\phi e^{-\int \frac{d\mathbf{r}}{8\pi \ell_B} (\nabla \phi)^2} \quad (\text{A5})$$

The technical details of the computation of F_3 can be found in Ref. [50]. The last term of Eq. (A5) simply corresponds to the free energy of a bulk electrolyte with a dielectric constant ϵ_w . In the above relations, S stands for the lateral area of the system. The dummy ‘‘charging’’ parameter ξ is usually introduced to compute the Debye-Hückel free energy [51]. It multiplies the Debye lengths of $\hat{v}_0(z, z, \mathbf{k}; \kappa_v(z))$ in Eq. (A4) and the dielectric permittivities contained in the thermal average of the gradient in Eq.(A5). This later is defined as

$$\langle (\nabla \phi)^2 \rangle_\xi = -(\nabla \phi_0)^2 + \int \frac{d\mathbf{k}}{(2\pi)^2} (k^2 + \partial_z \partial_{z'}) \hat{v}_c[z, z', \mathbf{k}; \ell_\xi(z)]|_{z=z'} \quad (\text{A6})$$

where we have introduced $\ell_\xi^{-1}(z) \equiv \ell_B^{-1} + \xi [\ell_B^{-1}(z) - \ell_B^{-1}]$ and $\hat{v}_c[z, z', \mathbf{k}; \ell_\xi(z)]$ stands for the Fourier transformed Coulomb operator given by Eq. (5) with Bjerrum length $\ell_\xi(z)$. The quantity F_3 defined in Eq. (A5) does not depend on the inverse screening length κ_v . Moreover, in order to satisfy the electroneutrality, $\phi_0(z)$ must be constant in the salt-free parts of the system where $\ell_B(z) \neq \ell_B$. Hence, F_3 does not depend on the potential $\phi_0(z)$.

Appendix B: Variational choice for the neutral dielectric interface

We report in this appendix the restricted variational piecewise $\phi_0(z)$ for a neutral dielectric interface which is a solution of

$$\frac{\partial^2 \phi_0}{\partial z^2} = 0 \quad \text{for } z \leq a \quad (\text{B1})$$

$$\frac{\partial^2 \phi_0}{\partial z^2} - \kappa_\phi^2 \phi_0 = c z e^{-\kappa_\phi z} \quad \text{for } z \geq a \quad (\text{B2})$$

where $\phi_0(z)$ in both regions is joined by the continuity conditions

$$\phi_0^<(a) = \phi_0^>(a), \quad \left. \frac{\partial \phi_0^<}{\partial z} \right|_{z=a} = \left. \frac{\partial \phi_0^>}{\partial z} \right|_{z=a}. \quad (\text{B3})$$

We also tried to introduce different variational screening lengths in the second term of the lhs. and in the rhs. of Eq. (B2) without any significant improvement at the variational level. For this reason, we opted for a single

inverse variational screening length, κ_ϕ . The solution of Eqs. (B1)-(B2) is

$$\phi_0(z) = \begin{cases} \varphi & \text{for } z \leq a, \\ \varphi [1 + \kappa_\phi(z - a)] e^{-\kappa_\phi(z-a)} & \text{for } z \geq a. \end{cases} \quad (\text{B4})$$

where the coefficient c disappears when we impose the boundary and continuity conditions, Eq. (B3). The remaining variational parameters are the constant potential φ , the distance a and the inverse screening length κ_ϕ . By substituting Eq. (B4) into Eq. (A3), we obtain the variational grand potential

$$F_v = V \frac{\kappa_b^3}{24\pi} + \frac{S}{32\pi} \left(\Delta\kappa_b^2 - \frac{\kappa_\phi}{\ell_B} \varphi^2 \right) - S\rho_- \int_0^\infty dz \times \left\{ e^{-\frac{q_-^2}{2} w(z) + q_- \phi_0(z)} + \frac{q_-}{q_+} e^{-\frac{q_+^2}{2} w(z) - q_+ \phi_0(z)} \right\} \quad (\text{B5})$$

Appendix C: Variational choice for the charged dielectric interface

The two types of piecewise variational functions used for single charged surfaces are reported below.

- The first trial potential obeys the salt-free equation in the first zone and the NLPB solution in the second zone,

$$\begin{aligned} \frac{\partial^2 \tilde{\phi}_0^{\text{NL}}}{\partial \tilde{z}^2} &= 2\delta(\tilde{z}) \quad \text{for } \tilde{z} \leq \tilde{h}, \\ \frac{\partial^2 \tilde{\phi}_0^{\text{NL}}}{\partial \tilde{z}^2} - \tilde{\kappa}_\phi^2 \sinh \phi_0 &= 0 \quad \text{for } \tilde{z} \geq \tilde{h}, \end{aligned} \quad (\text{C1})$$

whose solution is

$$\tilde{\phi}_0^{\text{NL}}(\tilde{z}) = \begin{cases} 4\text{arctanh}\gamma + 2(\tilde{z} - \tilde{h}) & \text{for } \tilde{z} \leq \tilde{h}, \\ 4\text{arctanh}\left(\gamma e^{-\tilde{\kappa}_\phi(\tilde{z} - \tilde{h})}\right) & \text{for } \tilde{z} \geq \tilde{h}, \end{cases} \quad (\text{C2})$$

where $\gamma = \tilde{\kappa}_\phi - \sqrt{1 + \tilde{\kappa}_\phi^2}$. Variational parameters are h and κ_ϕ , and the electrostatic contribution of the variational grand potential Eq. (A3) is

$$\frac{F_1}{\tilde{S}} = \frac{\tilde{h} + \gamma - 4\text{arctanh}\gamma}{2\pi\Xi} - \frac{\tilde{\kappa}_b^2}{4\pi\Xi} \int d\tilde{z} e^{-\frac{\Xi}{2}\tilde{w}(\tilde{z})} \cosh \tilde{\phi}_0^{\text{NL}}. \quad (\text{C3})$$

- The second type of trial potential obeys the salt-free equation with a charge renormalization in the first zone and the linearized Poisson-Boltzmann solution in the second zone,

$$\begin{aligned} \frac{\partial^2 \tilde{\phi}_0^{\text{L}}}{\partial \tilde{z}^2} &= 2\eta\delta(\tilde{z}) \quad \text{for } \tilde{z} \leq \tilde{h}, \\ \frac{\partial^2 \tilde{\phi}_0^{\text{L}}}{\partial \tilde{z}^2} - \tilde{\kappa}_\phi^2 \tilde{\phi}_0^{\text{L}} &= 0 \quad \text{for } \tilde{z} \geq \tilde{h}, \end{aligned} \quad (\text{C4})$$

whose solution is given by

$$\tilde{\phi}_0^{\text{L}}(\tilde{z}) = \begin{cases} -\frac{2\eta}{\tilde{\kappa}_\phi} + 2\eta(\tilde{z} - \tilde{h}) & \text{for } \tilde{z} \leq \tilde{h}, \\ -\frac{2\eta}{\tilde{\kappa}_\phi} e^{-\tilde{\kappa}_\phi(\tilde{z} - \tilde{h})} & \text{for } \tilde{z} \geq \tilde{h}. \end{cases} \quad (\text{C5})$$

Variational parameters introduced in this case are \tilde{h} , $\tilde{\kappa}_\phi$, and the charge renormalization η , which takes into account non-linearities at the mean-field level [19]. The variational grand potential reads

$$\begin{aligned} \frac{F_1}{\tilde{S}} &= \frac{2\eta(1 + \tilde{h}\tilde{\kappa}_\phi) - \eta^2(1/2 + \tilde{h}\tilde{\kappa}_\phi)}{2\pi\Xi\tilde{\kappa}_\phi} \\ &\quad - \frac{\tilde{\kappa}_\phi^2}{4\pi\Xi} \int d\tilde{z} e^{-\frac{\Xi}{2}\tilde{w}(\tilde{z})} \cosh \tilde{\phi}_0^{\text{L}}(\tilde{z}). \end{aligned} \quad (\text{C6})$$

In both cases, the boundary condition satisfied by ϕ_0 is the Gauss law

$$\left. \frac{\partial \tilde{\phi}_0}{\partial \tilde{z}} \right|_{z=0} = 2\eta \quad (\text{C7})$$

where $\eta = 1$ for the non-linear case. It is important to stress that in the case of a charged interface, Eq. (C7) holds even if $\epsilon \neq 0$. In fact, since the left half-space is ion-free, $\tilde{\phi}_0(z)$ must be constant for $z < 0$ in order to satisfy the global electroneutrality in the system.

Appendix D: Definition of the special functions

The definition of the four special functions used in this work are reported below.

$$\text{Li}_n(x) = \sum_{k \geq 1} \frac{x^k}{k^n}, \quad \xi(n) = \text{Li}_n(1) \quad (\text{D1})$$

$$\beta(x; y, z) = \int_0^x dt t^{y-1} (1-t)^{z-1} \quad (\text{D2})$$

$${}_2F_1(a, b; c; x) = \sum_{k \geq 0} (a)_k (b)_k (c)_k \frac{x^k}{k!} \quad (\text{D3})$$

where $(a)_k = a!/(a-k)!$.

Appendix E: Disjoining pressure for the neutral pore

The net pressure between plates is defined as

$$P = -\frac{1}{S} \frac{\partial F_v}{\partial d} - \left(2\rho_b - \frac{\kappa_b^3}{24\pi} \right) \quad (\text{E1})$$

where the subtracted term on the rhs. is the pressure of the bulk electrolyte. The total van der Waals free energy, which is simply the zeroth order contribution F_0 to the variational grand potential Eq. (9), is with the

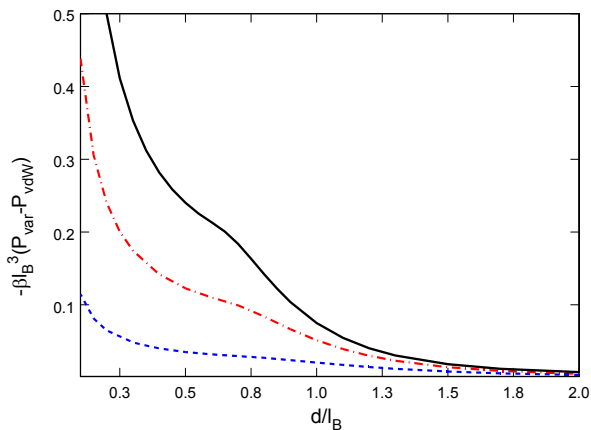


FIG. 17: (color online) Difference between the pressure and the screened van der Waals contribution vs d/l_B for $\kappa_b l_B = 0.5, 1$ and 1.5 , from left to right ($\epsilon = 0$).

constraint $\kappa_v = \kappa_b$ (there is no renormalization of the

inverse screening length at this order),

$$F_{\text{vdW}} = \frac{d\kappa_b^3}{24\pi} - \frac{\kappa_b}{8\pi d} \text{Li}_2(e^{-2d\kappa_b}) - \frac{1}{16\pi d^2} \text{Li}_3(e^{-2d\kappa_b}) \quad (\text{E2})$$

and

$$P_{\text{vdW}} = -\frac{1}{S} \frac{\partial F_{\text{vdW}}}{\partial d} + \frac{\kappa_b^3}{24\pi}. \quad (\text{E3})$$

We illustrate in Fig. 17 the difference between the van der Waals pressure and the prediction of the variational calculation for $\kappa_b l_B = 0.5, 1$ and 1.5 . We notice that the prediction of our variational calculation yields a very similar behavior to that illustrated in Fig. 8 of Ref. [21]. The origin of the extra-attraction that follows from the variational calculation was discussed in detail in the same article. This effect originates from the important ionic exclusion between the plates at small interplate separation, an effect that can be captured within the variational approach.

-
- [1] A. Heydweiller, Ann. d. Phys., **4**, 33145 (1910)
- [2] P.K. Weissenborn and R.J. Pugh, Langmuir, **11**, 1422 (1995)
- [3] G. Wagner, Phys. Zs., **25**, 474 (1924)
- [4] L. Onsager and N. Samaras, J. Chem. Phys., **2** 528 (1934)
- [5] V.E. Bravina, Soviet phys. Doklady, **120**, 381 (1958)
- [6] A.E. Yaroshchuk, Adv. Colloid Interf. Sci., **85**, 193 (2000)
- [7] R.B. Schoch, J. Han and P. Renaud, Rev. Mod. Phys. **80**, 839 (2008)
- [8] A.G. Moreira and R.R. Netz, Phys. Rev. Lett., **87**, 078301 (2000)
- [9] A.G. Moreira and R.R. Netz, Europhys. Lett., **52**, 705 (2000)
- [10] H. Boroudjerdi *et al.*, Physics Reports, **416**, 129 (2005)
- [11] R.R. Netz and H. Orland, Eur. Phys. J. E, **1**, 203 (2000)
- [12] A.G. Moreira and R.R. Netz, Eur. Phys. J. E, **8**, 33 (2002)
- [13] A. Naji, S. Jungblut, A. Moreira and R.R. Netz, Physica A, **352**, 131 (2005)
- [14] S. Alexander, P.M. Chaikin, P. Grant, G.J. Morales, P. Pincus and D. Hone, J. Chem. Phys., **80**, 5776 (1984)
- [15] Levin Y., Rep. Prog. Phys., **65**, 1577 (2002)
- [16] Levin Y., J. Chem. Phys., **113**, 9722 (2000)
- [17] G.S. Manning, J. Chem. Phys., **51**, 924 (1969)
- [18] M. Kanduc, A. Naji, Y.S. Jho, P.A. Pincus and R. Podgornik, J. Phys.: Condens. Matter, **21**, 424103 (2009)
- [19] R.R. Netz and H. Orland, Eur. Phys. J. E, **11**, 301 (2003)
- [20] R.A. Curtis and L. Lue, J. Chem. Phys., **123**, 174702 (2005)
- [21] M.M. Hatlo, R.A. Curtis and L. Lue, J. Chem. Phys., **128**, 164717 (2008)
- [22] M.M. Hatlo and L. Lue, Soft Matter, **4**, 1582 (2008)
- [23] M.M. Hatlo and L. Lue, Soft Matter, **5**, 125 (2009)
- [24] R.R. Netz, Eur. Phys. J. E, **5**, 557 (2001)
- [25] The case with dielectric discontinuity has been studied without added salt in M.M. Hatlo and L. Lue, arXiv:0806.3716, (2008)
- [26] V.M. Starov and N.V. Churaev, Adv. Colloid Interf. Sci. **43**, 145 (1993)
- [27] X. Lefebvre, J. Palmeri and P. David, J. Phys. Chem. B **108**, 16811 (2004)
- [28] A. Yaroshchuk, Sep. Purif. Technology 22-23, 143 (2001)
- [29] C. Li and H. R. Ma, J. Chem. Phys., **121**, 1917 (2004)
- [30] I. Benjamin, Annu. Rev. Phys. Chem., **48**, 407-51 (1997)
- [31] S.M. Avdeev and G.A. Martynov. Colloid J. USSR, **48**, 632 (1968)
- [32] Note that the factor Ξ^{-1} in front of v_0 in Eq. (12) found in [19] should be cancelled.
- [33] J. Janeček and R.R. Netz, J. Chem. Phys., **130**, 074502 (2009)
- [34] This is in fact a *maximization* with respect to ϕ_0 or to any variational parameter associated to a restricted choice for ϕ_0 . Indeed, the physical electrostatic potential ϕ_0 corresponds to a pure imaginary auxiliary field ϕ in the functional integral \mathcal{Z} . Hence the (complex) minimum of $\langle H - H_0 \rangle_0$ with respect to ϕ corresponds to a (real) maximum with respect to ϕ_0 .
- [35] J.D. Jackson, *Classical Electrodynamics* (Wiley 2nd ed., New York, 1975)
- [36] A. Szymczyk and P. Fievet, J. Membrane Sci. **252**, 77 (2005)
- [37] F. Fornasiero *et al.*, Proc. Nat. Acad. Sci. USA, **105**, 17250 (2008)
- [38] X. Lefebvre and J. Palmeri, J. Phys. Chem. B **109**, 5525 (2005)
- [39] A. Yaroshchuk, Adv. Colloid Interf. Sci. **60** 1 (1995)
- [40] M.E. Fisher and Y. Levin, Phys. Rev. Lett., **71**, 3826 (1993)
- [41] J.P. Simonin *et al.*, J. Phys Chem. B, **103**, 699 (1999)
- [42] S. Senapati and A. Chandra, J. Phys. Chem. B, **105**, 5106 (2001)
- [43] J. Marti *et al.*, J. Phys. Chem. B, **110**, 23987 (2006)

- [44] S. Buyukdagli, D.S. Dean, M. Manghi and J. Palmeri, in preparation.
- [45] P. Jungwirth and B. Winter, *Annu. Rev. Phys. Chem.*, **59**, 343 (2008)
- [46] C.D. Lorenz and A. Travasset, *Phys. Rev. E*, **75**, 061202 (2007)
- [47] A. Naji and R. Podgornik, *Phys. Rev. E*, **72**, 041402 (2005)
- [48] Y. Ge *et al.*, *Phys. Rev. E*, **80**, 021928 (2009)
- [49] K. Leung and S.B. Rempe, *J. Comput. Theoret. Nanosci.*, **6**, 1948 (2009)
- [50] R.R. Netz, *Eur. Phys. J. E*, **5**, 189 (2001)
- [51] D.A. McQuarrie, *Statistical Mechanics* chap.15 (University Science Book, New York, 2000)